Astronomy
&
Astrophysics

ISO spectroscopy of compact H II regions in the Galaxy⋆

II. Ionization and elemental abundances

N. L. Martín-Hernández[1], E. Peeters[2,1], C. Morisset[3], A. G. G. M. Tielens[1,2], P. Cox[4], P. R. Roelfsema[2], J.-P. Baluteau[3], D. Schaerer[5], J. S. Mathis[6], F. Damour[3], E. Churchwell[6], and M. F. Kessler[7]

[1] Kapteyn Institute, PO Box 800, 9700 AV Groningen, The Netherlands
[2] SRON, National Institute for Space Reasearch, PO Box 800, 9700 AV Groningen, The Netherlands
[3] Institut d'Astrophysique de Marseille, CNRS & Univ. de Provence, BP 8, 13376 Marseille Cedex 12, France
[4] Institut d'Astrophysique Spatiale, Bât. 121, Université de Paris XI, 91405 Orsay, France
[5] Laboratoire d'Astrophysique, Observatoire Midi-Pyrénées, 14, Av. E. Belin, 31400 Toulouse, France
[6] Department of Astronomy, 475 North Charter Street, University of Wisconsin, Madison, WI 53706, USA
[7] ISO Data Centre, Astrophysics Division, ESA, Villafranca, Spain

Abstract. Based on the ISO spectral catalogue of compact H II regions by Peeters et al. (2002), we present a first analysis of the hydrogen recombination and atomic fine-structure lines originated in the ionized gas. The sample consists of 34 H II regions located at galactocentric distances between $R_{\rm Gal} = 0$ and 15 kpc. The SWS H I recombination lines between 2 and 8 μm are used to estimate the extinction law at these wavelengths for 14 H II regions. An extinction in the K band between 0 and ∼3 mag has been derived. The fine-structure lines of N, O, Ne, S and Ar are detected in most of the sources. Most of these elements are observed in two different ionization stages probing a range in ionization potential up to 41 eV. The ISO data, by itself or combined with radio data taken from the literature, is used to derive the elemental abundances relative to hydrogen. The present data thus allow us to describe for each source its elemental abundance, its state of ionization and to constrain the properties of the ionizing star(s). The main results of this study are as follows. The ionization ratios Ar^{++}/Ar^+, N^{++}/N^+, S^{+3}/S^{++} and Ne^{++}/Ne^+, which measure the degree of ionization and to first order, the hardness of the stellar radiation, seem to increase with $R_{\rm Gal}$. These ionization ratios correlate well with each other, implying that the spectral hardening affects equally the full range of ionizing energies. A Galactocentric gradient of N/O ($\Delta \log N/O = -0.056 \pm 0.009$ dex kpc^{-1}) is observed in the sense of a decreasing abundance ratio with $R_{\rm Gal}$ in agreement with previous studies. Abundance gradients for neon and argon are derived of the form $\Delta \log Ne/H = -0.039 \pm 0.007$ dex kpc^{-1} and $\Delta \log Ar/H = -0.045 \pm 0.011$ dex kpc^{-1}. These elemental gradients could be enlarged by the existing Galactic $T_{\rm e}$ gradient. Adopting a $T_{\rm e}$ gradient of approximately 330 K kpc^{-1}, the slopes in the Ne/H and Ar/H gradients become -0.06 and -0.07 dex kpc^{-1}, respectively. Lower limits for the sulphur and oxygen abundances are derived. Nitrogen abundances are derived for 16 sources.

Key words. ISM: abundances – ISM: dust, extinction – ISM: H II regions – galaxy: abundances – infrared: ISM: lines – atomic data

1. Introduction

The distribution of Galactic elemental abundances is central to study the chemical evolution of the Milky Way. The relative abundances of the elements are sensitive to the star formation history, the number of massive stars, the relative yield of the elements, and the exchange of matter between the disk and the halo through infall or ejection. Measurements of elemental abundances throughout the Galactic disk thus provide vital inputs to model the formation and evolution of the Galaxy.

H II regions are prime targets to derive the present-day elemental abundances. These objects consist of gas which is ionized and heated by the radiation of massive stars. When the massive ionizing star is newly formed, it is still embedded in its natal molecular cloud and the

resulting H II, region is a young, bright and compact nebula. Measuring the elemental abundances of the ionized gas in H II regions allows us to probe the interstellar medium (ISM) in the vicinity of massive stars and to trace the present composition of the ISM in the Galaxy.

Abundance determination methods based on infrared observations present clear advantages over optical studies because the infrared fine-structure lines are not very sensitive to changes in the electron temperature and do not suffer from high extinction. Infrared measurements can thus trace the elemental abundances in the central regions of the Galaxy. The infrared is also the only wavelength regime to measure the N^{++} ion, the dominant form of nitrogen in highly ionized H II regions.

Previous determinations of the Galactic distribution of elemental abundances based on the study of H II regions have been performed in the optical (Shaver et al. 1983; Fich & Silkey 1991; Deharveng et al. 2000) and in the infrared, based on IRAS (Simpson & Rubin 1990) and Kuiper Airborne Observatory (KAO) observations (Lester et al. 1987; Rubin et al. 1988; Simpson et al. 1995b; Afflerbach et al. 1997; Rudolph et al. 1997). These studies resulted in a series of firm results concerning the variation of elemental abundances across the Galaxy: the electron temperature (T_e) of the H II regions increases with R_{Gal}; the abundance ratio N/O decreases with R_{Gal}; the abundances of the heavy elements N, O, Ne, S, and Ar decrease with R_{Gal}. Additional optical studies are based on photospheric emission lines from B stars (Fitzsimmons et al. 1992; Smartt & Rolleston 1997; Gummersbach et al. 1998; Rolleston et al. 2000; Smartt et al. 2001) and on planetary nebulae (Maciel & Koppen 1994; Maciel & Quireza 1999). Similar results and gradients have been derived towards other galaxies (e.g. Vila-Costas & Edmunds 1992; Zaritsky et al. 1994).

The Infrared Space Observatory (ISO) spectral catalogue of compact H II regions (Peeters et al. 2002, hereafter Paper I) presents the combined Short Wavelength Spectrometer (SWS) and Long Wavelength Spectrometer (LWS) grating spectra from 2.3 to 196 μm for 43 nebulae. The catalogue tabulates the fluxes for the hydrogen recombination and atomic fine-structure lines. A detailed explanation on the error of these line fluxes, which will be used in the present paper, is given in Sect. 4 of the catalogue. The spectral coverage gives access to nearly all the atomic fine-structure lines in the infrared range. Lines from the elements C, O, N, S, Ne, Si and Ar are present in most of the sources. This paper will concentrate on the lines emitted by the ionized gas in the H II region. The [C II], [O I] and [Si II] lines, produced by ions with ionization potentials lower than 13.6 eV, are expected to be mostly emitted in the Photodissociation Region (PDR) and will be analyzed by Damour et al. (in prep.). For some of the ions (O^{++}, Ne^{++} and S^{++}) two lines are present providing, in principle, an estimate of the electron density. All the elements except for oxygen (note that O^0, as mentioned above, is produced in the PDR) are observed in two ionization stages (see Fig. 1), which alleviates the problem of

applying ionization correction factors for unseen ions (especially for S, Ne and Ar). Finally, the range of ionization potential covered by this set of data (up to 41 eV) allows us to examine the ionization state of the H II regions and to constrain the properties of the ionizing star(s). From the whole sample, 34 H II regions present enough emission lines to determine their elemental abundances and ionization properties. This subsample covers the Galactic plane from the centre to a galactocentric distance, R_{Gal}, of 15 kpc. It is thus possible to investigate trends of the ionization conditions in H II regions and of relative and absolute abundances across a large part of the Galactic disk. Atomic parameters are crucial in order to interpret correctly the strengths of the different lines. The latest transition probabilities and collisional strengths have been compiled (cf. Table 1) and used throughout this paper.

This paper is structured as follows. Section 2 describes the kinematic distances and radio properties of the H II regions; Sect. 3 discusses the problem of extinction; a discussion of the densities of the H II regions is given in Sect. 4; Sect. 5 gives an outline of the methodology used to derive elemental abundances with a particular emphasis on the advantages/disadvantages of the present data; Sect. 6 presents the results for the ionization state and its variation with galactocentric distance. The ionic and elemental abundances, and their variation with R_{Gal}, are presented in Sect. 7; finally, Sect. 8 discusses and summarizes the results of this paper.

Table 1. References for the transition probabilities A and the collisional stengths Ω used in this paper. IP refers to the IRON project.

| Species		Reference
N II	A:	Galavís et al. (1997) (IP XXII)
	Ω:	Lennon & Burke (1994) (IP II)
N III	A:	Galavís et al. (1998a) (IP XXIX)
	Ω:	Blum & Pradhan (1992)
O III	A:	Galavís et al. (1997) (IP XXII)
	Ω:	Lennon & Burke (1994) (IP II)
Ne II	A:	Mendoza (1983)
	Ω:	Saraph & Tully (1994) (IP IV)
Ne III	A:	Galavís et al. (1997) (IP XXII)
	Ω:	Butler & Zeippen (1994) (IP V)
S III	A:	Biemont & Bromage (1983)
	Ω:	Tayal & Gupta (1999)
S IV	A:	Mendoza (1983)
	Ω:	Saraph & Storey (1999) (IP XXX)
Ar II	A:	Mendoza (1983)
	Ω:	Pelan & Berrington (1995) (IP IX)
Ar III	A:	Mendoza & Zeippen (1983)
	Ω:	Galavís et al. (1995) (IP X)
		Galavís et al. (1998b) (IP XXXII)
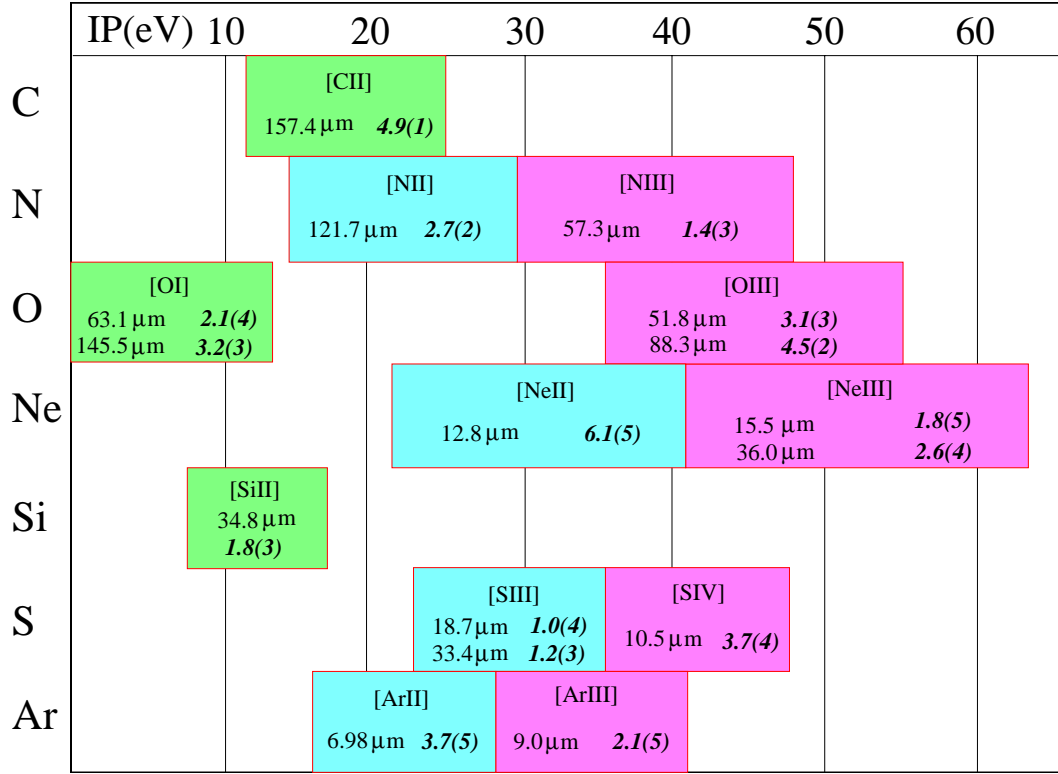
Fig. 1. The fine-structure atomic lines observed in the combined ISO SWS/LWS spectra of compact H II regions are shown as a function of the ionization potential. The electron critical densities, indicated for every line in italic, are given in units of cm^{-3} and are expressed as $a(b) = a \times 10^b$. The critical densities for the ions with ionization potential lower than 13.6 eV (emitted in the photodissociation region) are taken from Tielens & Hollenbach (1985). The other critical densities were calculated using the latest atomic parameters (see Table 1).

2. Distances and radio properties

2.1. Kinematic distances

The study of the elemental abundance variation from atomic fine-structure lines emitted by H II regions relies on proper determinations of the galactic distances to the H II regions and in this sense, a detailed literature study has been done in order to get the most accurate distances to the program sources.

The determination of the distances to the H II regions of the ISO sample has been discussed in Paper I and the reader is referred to this paper for detailed information. Table 2 lists in Cols. 2 and 3 the adopted distances R_{Gal} and $R_{\odot}$ (including in the latter the near and far solar distances).

2.2. Radio properties

Radio continuum measurements allow one to derive various properties of the H II regions such as the emission measure (EM), rms electron density ($n_{\text{e,rms}}$) and the Lyman continuum photon flux (N_{Lyc}). These parameters can be derived for spherical sources if the radio flux density and the source size are known. For non-spherical sources, the geometrical average of the major and minor axes can be taken as a representative size.

In the Rayleigh-Jeans limit, the brightness temperature, T_{b}, can be estimated from:

$$T_{\text{b}} = \frac{10^{-23} c^2 S_\nu}{2\nu^2 k \Omega} \ [\text{K}], \tag{1}$$

where S_ν is the integrated flux density in Jy, ν is the frequency in Hz and Ω is the source solid angle in sr. The optical depth for an ionized, optically thin gas at a temperature T_{e} is given by:

$$T_{\text{b}} = T_{\text{e}}(1 - e^{-\tau}) \sim T_{\text{e}}\tau \ . \tag{2}$$

The emission measure can be derived from τ using:

$$EM = \frac{\tau}{8.235 \times 10^{-2} a_\nu \left(\frac{T_{\text{e}}}{\text{K}}\right)^{-1.35} \left(\frac{\nu}{\text{GHz}}\right)^{-2.1}} \ [\text{pc cm}^{-6}], \tag{3}$$

where a_ν is a correction factor close to unity (Mezger & Henderson 1967).

To estimate the rms electron density we used the formalism explained by Wood & Churchwell (1989):

$$n_{\text{e,rms}} = \sqrt{\frac{EM[\text{pc cm}^{-6}]}{\Delta s[\text{pc}]}} \ [\text{cm}^{-3}] \ , \tag{4}$$

where Δs is the path length of the emitting region (taken as the source size). Finally, the photon flux of the Lyman continuum can be determined from:

$$N_{\text{Lyc}} = 1.54 \times 10^{55} (n_{\text{e,rms}})^2 \left(\frac{\Delta s}{\text{pc}}\right)^3 \alpha_{\text{B}} \ [\text{s}^{-1}] \ , \tag{5}$$

Table 2. Kinematic distances and radio properties of the sample sources.

Source	$R_{\rm gal}$ (kpc)	$R_{\odot}$ [a] (kpc)	λ (cm)	S_{ν} (mJy)	Size ($''$)	EM (10^6 pc cm^{-6})	$n_{\rm e,rms}$ [b] (10^3 cm^{-3})	$\log N_{\rm Lyc}$ [b] (s^{-1})	Ref.
IR 01045	13.8	7.0	6	290	3	14.5	11.9	47.9	1,2
IR 02219	11.0	3.3	6	25 000	35	9.2	4.0	49.2	3,4
IR 10589	9.5	8.0	-	-	-	-	-	-	-
IR 11143	9.7	8.8	-	-	-	-	-	-	-
IR 12063	9.3	9.5	-	-	-	-	-	-	-
IR 12073	10.1	10.8	-	-	-	-	-	-	-
IR 12331	6.9	4.5	-	-	-	-	-	-	-
IR 15384	6.4	2.7 (11.5)	-	-	-	-	-	-	-
IR 15502	4.6	6.0 (8.4)	-	-	-	-	-	-	-
IR 16128	5.5	3.7 (11.4)	-	-	-	-	-	-	-
IR 17160	3.0	5.7 (11.0)	6	1300	12	4.0	3.5 (2.5)	48.4 (48.9)	5
IR 17221	5.2	3.4 (13.4)	-	-	-	-	-	-	-
IR 17279	3.4	5.1 (11.8)	6	161	10	0.7	1.7 (1.1)	47.3 (48.1)	5
Sgr C	0.3	8.2 (8.8)	21	6400	120	0.2	0.2 (0.2)	49.3 (49.4)	6
IR 17455	0.5	8.0 (9.0)	6	1600	14	3.7	2.6 (2.4)	48.7 (48.8)	5,7
IR 17591	5.5	3.0 (13.8)	6	1310	8	9.2	8.9 (4.1)	47.8 (49.1)	7
IR 18032	7.6	1.0 (15.8)	6	640	15	1.3	4.2 (1.1)	46.5 (48.9)	7
IR 18116	4.3	4.5 (12.0)	6	3860	20	4.3	3.1 (1.9)	48.6 (49.5)	7
IR 18162	6.6	1.9 (14.7)	6	4	5	0.07	1.3 (0.5)	44.9 (46.7)	1
IR 18317	4.5	4.9 (10.6)	6	1290	13	3.4	3.3 (2.3)	48.2 (48.9)	5
IR 18434	4.6	5.7 (9.0)	6	2280	7	20.9	10.4 (8.3)	48.6 (49.0)	5
IR 18469	4.8	5.3 (9.2)	6	102	13	0.3	0.9 (0.7)	47.2 (47.7)	5
IR 18479	7.5	1.2 (13.1)	6	2030	7	18.6	21.4 (6.5)	47.2 (49.3)	5
IR 18502	4.7	7.1	6	1090	6	13.6	8.1 (2.2)	48.5 (50.8)	7
IR 19207	6.1	5.7	21	13 700	140	0.3	0.3 (0.1)	49.3 (51.8)	8
IR 19442	7.6	2.5 (5.8)	6	23	1	10.3	29.2 (19.2)	45.9 (46.6)	9
IR 19598	9.8	8.5	3.6	3475	6	45.6	13.6	49.1	10
DR 21	8.6	2.8	6	17 500	20	19.6	8.5	48.9	11
IR 21190	12.7	8.9	6	906	4	25.4	12.1	48.6	12
IR 21270	14.8	11.3	6	563	120	0.02	0.1	48.6	13
IR 21306	12.6	8.3	-	-	-	-	-	-	-
IR 22308	11.3	5.5	6	554	90	0.03	0.1	48.0	13
IR 23030	11.4	5.2	6	1900	40	0.5	0.7	48.4	14
IR 23133	11.7	5.5	6	1048	15	2.1	2.3	48.2	14

[a] Value in brackets is the far solar distance.
[b] Two different values are derived for sources within the solar circle because of the near-far solar distance ambiguity. Values in brackets are calculated using the far solar distance.
REFERENCES: (1) McCutcheon et al. (1991), (2) Rudolph et al. (1996), (3) Roelfsema & Goss (1991), (4) Tieftrunk et al. (1997), (5) Becker et al. (1994), (6) Liszt & Spiker (1995), (7) Garay et al. (1993), (8) Mehringer (1994), (9) Barsony (1989), (10) Afflerbach et al. (1996), (11) Roelfsema et al. (1989), (12) Isaacman (1984), (13) Fich (1993), (14) Fich (1986).

where $\alpha_{\rm B} = 3.28 \times 10^{-13}$ cm^3 s^{-1} (Hummer & Storey 1987) is the case B recombination coefficient of hydrogen to all levels $n \geq 2$ (for $T_{\rm e} = 7500$ K).

Flux densities and source sizes were taken from the literature selecting observations made at frequencies larger than 5 GHz. This ensures that the emission is optically thin. In addition, care was taken to select observations with a spatial resolution of the order of a few arcseconds to avoid structures larger than $10''$ to be resolved out.

Radio properties derived using the above equations are listed in Table 2 for those sources with published observations satisfying the above requirements.

3. Extinction

Compact H II regions are heavily embedded in dust and gas and suffer a dimming of their radiation by dust located either within the ionized gas or in the neutral foreground

material. The term "extinction" usually refers to the dimming of starlight, for which scattering from the beam contributes as much as true absorption because the star is effectively a point source. For extended objects, the scattering is less effective in attenuating the radiation because photons can be scattered into the beam as well as out of it. The effectiveness of scattering depends upon the geometry of the sources relative to the dust. In our objects, this is unknown. Hence, we will refer to the dimming of our objects due to dust absorption as "extinction" throughout this paper.

The extinction towards compact H II regions is generally high with values of A_V ranging from $\sim$10 to hundreds of magnitudes – corresponding to extinction of $\sim$1 to a few 10 mag at near- and mid-infrared wavelengths. The extinction in the far-infrared is generally negligible. For a number of H II regions, the ISO SWS spectra show a series of H I recombination lines which can be used to derive the extinction curve characterizing the dust absorption towards these sources. Radio continuum emission can also be used to derive the expected flux at any H I recombination line to provide an alternative estimate of the extinction when comparing with the observed line flux.

3.1. HI recombination lines method

The mid-infrared H I recombination lines from the Brackett ($n \to 4$), Pfund ($n \to 5$) and Humphreys ($n \to 6$) series between 2 and 8 μm can be used to derive the extinction law at these wavelengths by comparing the ratio of observed line strengths to the predictions of recombination theory assuming a nebular electron density, n_e, and temperature, T_e. The ratio of the hydrogen emission coefficients is not very sensitive to n_e or T_e. Therefore, we have adopted $n_e = 1000$ cm^{-3} and $T_e = 7500$ K, which are typical values for H II regions. In the following, we will consider the standard case B treatment, ie. where the nebula is optically thick to the Lyman series photons but optically thin to all other series photons (see, e.g., Osterbrock 1989). The observed line flux, $F(\lambda)$, can then be expressed as:

$$F(\lambda) = F_o(\lambda)10^{-0.4A_\lambda} , \qquad (6)$$

where $F_o(\lambda)$ is the non-extincted line flux, given by case B theory, and A_λ is the extinction at the wavelength λ. The relative extinction to a reference line (e.g. Brα at 4.05 μm) is:

$$A_\lambda - A_{\mathrm{Br}\alpha} = -2.5 \left(\log \frac{F(\lambda)}{F(\mathrm{Br}\alpha)} - \log \frac{F_o(\lambda)}{F_o(\mathrm{Br}\alpha)} \right). \qquad (7)$$

The theoretical ratios are taken from Hummer & Storey (1987).

Figure 2 shows the relative extinction $A_\lambda - A_{\mathrm{Br}\alpha}$ derived for the H II regions which have at least 3 H I recombination lines (14 sources in total) within the SWS range. The line fluxes are taken from Tables 7 and 8 in Paper I.

At infrared wavelengths longward of 1.25 μm, the extinction law, as based on JHK photometry, appears to be

Table 3. Extinction A_K as determined using the H I recombination lines method.

Source	A_K	Source	A_K	Source	A_K
IR 02219	1.5	IR 15502	2.7	IR 19598	1.6
IR 10589	1.5	IR 17221	1.8	IR 21190	0.0
IR 12063	0.8	IR 17455	1.8	IR 23030	0.0
IR 12073	0.8	IR 18317	2.0	IR 23133	0.0
IR 15384	1.3	IR 18434	1.6		

Table 4. Estimates of the extinctions A_λ/A_K to apply to the near- and mid-infrared lines using the "standard" extinction law described in the text.

Line	$\lambda(\mu m)$	A_λ/A_K	Line	$\lambda(\mu m)$	A_λ/A_K
Brβ	2.6	0.741	[Ne II]	12.8	0.165
Brα	4.0	0.354	[Ne III]	15.5	0.156
[Ar II]	7.0	0.140	[S III]	18.7	0.217
[Ar III]	9.0	0.429	[S III]	33.5	0.069
[S IV]	10.5	0.429	[Ne III]	36.0	0.060

independent of the line of sight and consistent with a simple power law $A_\lambda = A_K(\lambda/2.2)^{-1.7}$ (Mathis 1990; Martin & Whittet 1990), were A_K is the extinction in the K band (2.2 μm). For all the 14 sources we could derive an A_K for which this power law satisfies both the relative extinction at 2.62 μm (Brβ) and 4.05 μm (Brα). The solid lines in Fig. 2 show this power law for the corresponding A_K. Note that the curves generally fit the relative extinction at the other wavelengths nicely. The derived extinction values (A_K) are listed in Table 3.

From the computed A_K one can derive the extinction at other wavelengths using the results tabulated in Mathis (1990), namely $A_{9.7}/A_K = 0.544$ for the 9.7 μm silicate feature and $A_{18}/A_K = 0.217$ for the 18 μm silicate, in combination with the astronomical silicate profile of Draine (1985) and a λ^{-2} power law for $\lambda > 20$ μm. Using this "standard" extinction law, the extinction A_λ/A_K to apply to the near- and mid-infrared line fluxes is shown in Table 4. In contrast to the extinction between 2 and 7 μm, the extinction due to the silicate absorption at 9.7 and 18 μm depends on the line-of-sight (Draine 1989) and still both the shape and strength of these features remain controversial. Therefore, the "standard" extinctions for wavelengths longer than 7 μm given in Table 4 are merely illustrative and may not be applicable to all the H II regions.

Because of the lack of information on the extinction for most of the sample sources (extinction could only be derived for 14 sources out of 34) and the difficulties explained above in correcting the lines beyond 7 μm, *the line fluxes will not be corrected for extinction* in the analysis presented in this paper and instead the effect of the extinction will be indicated.
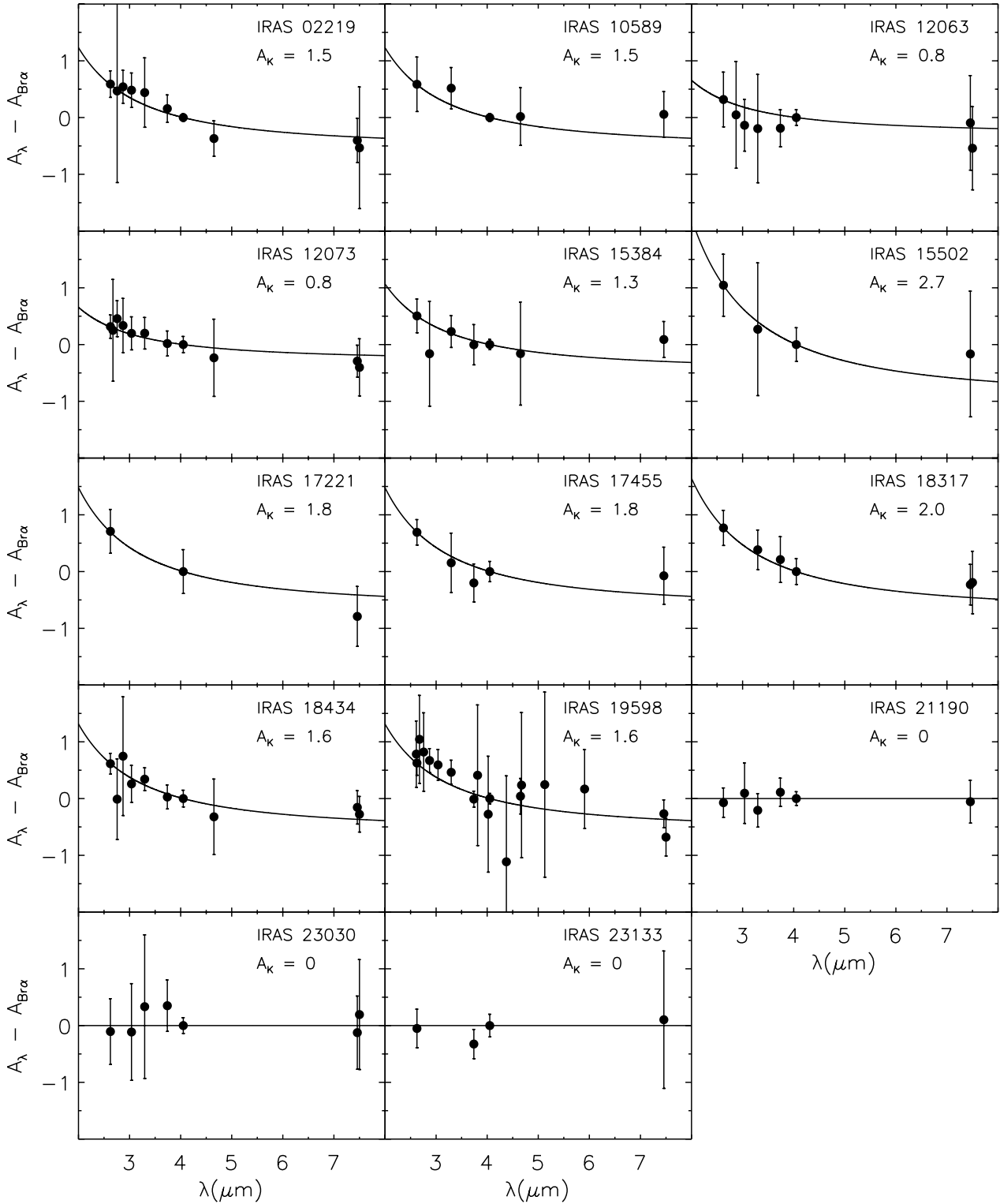
Fig. 2. Near- and mid-infrared extinction curves as derived from the H I recombination lines. Each panel is labeled by the name of the H II region and the derived extinction A_K. The solid lines show the extinction law (see Sect. 3.1).

3.2. Radio continuum method

The intrinsic flux of any H I recombination line can be determined if both T_e and the emission measure, EM, in the nebula are known. Radio continuum observations can provide this information (see Sect. 2). The intrinsic flux of Brα can be determined using:

$$F_{\mathrm{Br}\alpha} = \epsilon_{\mathrm{Br}\alpha} EM \left(\frac{n_{\mathrm{p}}}{n_{\mathrm{e}}} \right) \frac{\Omega}{4\pi}, \tag{8}$$
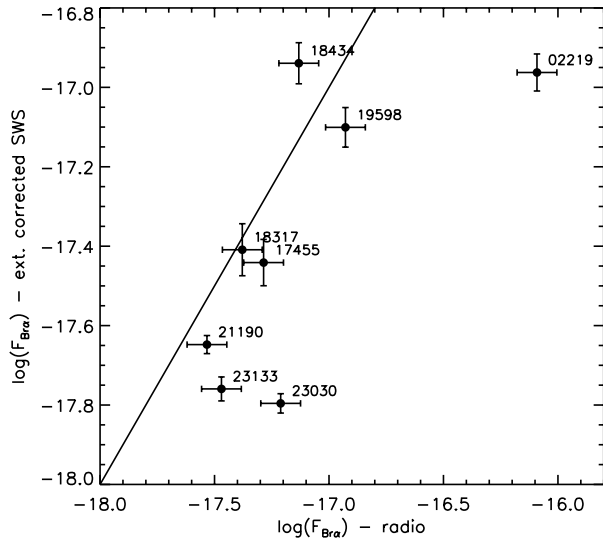
Fig. 3. Comparison between the Brα flux predicted by radio observations and the extinction-corrected Brα flux observed by SWS. The solid line represents the one-to-one relation.

where $\epsilon_{\text{Br}\alpha}$ is the emissivity of Brα and Ω is the solid angle of the source. Using Eqs. (1)–(3) and (8), the ratio of protons to electrons $n_{\text{p}}/n_{\text{e}} \approx 0.90$, $T_{\text{e}} = 7500\,\text{K}$ and $\epsilon_{\text{Br}\alpha} = 1.39 \times 10^{-26}\,\text{erg s}^{-1}\,\text{cm}^3$ (Hummer & Storey 1987), we obtain:

$$F_{\text{Br}\alpha} = 2.76 \times 10^{-18} \left(\frac{\nu}{\text{GHz}}\right)^{0.1} \left(\frac{S_{\nu}}{\text{Jy}}\right) \quad [\text{W cm}^{-2}], \qquad (9)$$

where the flux densities, S_{ν}, from Table 2 can be used. Figure 3 compares these predicted fluxes for Brα with the fluxes observed by SWS corrected using the extinction derived in Sect. 3.1. The radio flux densities and $A_{\text{Br}\alpha}$ are considered to have a nominal 20% uncertainty. In general, the radio Brα fluxes are larger than the extinction-corrected SWS fluxes, especially for IR 02219 and IR 23030. These two sources are much more extended in radio than the SWS beam (see Table 2). On the other hand, the predicted radio line flux for IR 18434 is slightly smaller. This source lies in a region of extended emission of up to a few arc-minutes (Kim & Koo 2001) which is observed by SWS and it is not included in the quoted radio flux density. This is probably the reason why the radio prediction leads to a lower line flux.

The application of predictions from radio continuum observations to our ISO data depends on the source geometry at both radio and infrared wavelengths and on the knowledge of the radio emission corresponding to the infrared emission observed by ISO.

3.3. Comments on individual sources

In the following, we comment on the extinction determination in individual H II regions from which previous studies are available.

IRAS 02219+6125 (W3 A) It is a very bright H II region located in a large 4′ by 3′ (Dickel et al. 1980) complex of H II regions, infrared sources and molecular clouds. Hayward et al. (1989) studied the extinction to W3 A by comparing the 5 GHz map by Harris & Wynn-Williams (1976) with their infrared (H and K) observations. They found that the extinction varies from $A_K \sim 1.0$ to 1.7, in agreement with our computed extinction ($A_K = 1.5$). The 9.7 μm extinction was studied by Hackwell et al. (1978), who found $A_{9.7}$ to vary from ~2.0 at the position of W3 A to ~4.0 at the perimeter of the W3 complex. This extinction due to the 9.7 μm silicate absorption is much larger than the $A_{9.7} = 0.8$ derived from our A_K when the "standard" extinction law described in Sect. 3.1 is used.

IRAS 12073−6233 Near-infrared slit observations by Armand et al. (1996) mapped the variation of several H I recombination lines across IRAS 12073−6233 and found A_K to vary from 1.2 to 1.7. We derive an extinction of $A_K = 0.8$ mag. The discrepancy in ~0.4−0.9 mag. can be caused by the fact that we have observed the integrated H I emission in a $14'' \times 20''$ beam, which may lead to a lower hydrogen density column because of the contribution of extended emission around the nebula and thus, to the lower extinction we obtain.

IRAS 18434−0242 (G29.96−0.02) It is one of the best studied ultracompact H II regions and classified as cometary (Wood & Churchwell 1989). By comparing images of the 2.17 μm Brγ recombination line and 2 cm radio continuum emission (Fey et al. 1995), Watson et al. (1997) derived a map of the extinction towards this H II region. They found that the apparent extinction to the nebula is not uniform, with A_K varying from 2.2 to 2.6 mag. They give a mean value $A_K = 2.14 \pm 0.25$. Pratap et al. (1999) estimated $A_K = 2.2 \pm 0.1$ towards the ionizing star based on its $H - K$ colour. As discussed above in the case of IRAS 12073−6233, the contribution of the extended envelope around the compact H II region (Kim & Koo 2001) to the SWS aperture may cause ISO to observe a lower hydrogen column density than the ones observed by the high ~1″ resolution observations of Watson et al. (1997) and Pratap et al. (1999). This could explain our lower $A_K = 1.6$ mag.

IRAS 19598+3324 (K3-50 A) It is the only H II region in the sample for which the SWS spectrum was also taken at speed 4, yielding a resolving power of ~1500 (see Paper I). In total, 20 H I recombination lines were detected (Tables 7 and 8 in Paper I) allowing us to derive a better sampled extinction curve in K3-50 A than for the other nebulae of the catalogue, especially in the region from 2 to 5 μm (Fig. 2). Note that the points around 3 μm seem to be slightly above the standard extinction curve, which could be due to the 3 μm O–H stretching mode seen in the spectrum (see Paper I). The extinction to K3-50 A

has been studied in detail by Howard et al. (1996) using both high-resolution near-infrared and radio images. They found variations in the extinction across the nebula. They reported an extinction at $4.05\,\mu$m (Brα) varying from 0 to 3 mag, with an averaged value of 1.6 in the central $2.7''$ region. This is the same value we get from the H I recombination lines analysis.

4. Density

The electron density ($n_{\rm e}$) can be determined from the ratio of two atomic fine-structure lines of the same ionic species when they are emitted from levels with nearly the same excitation energy (e.g. Rubin et al. 1994). This ratio is sensitive to gas densities approximately in between the critical densities of each line (see Fig. 1). A good indicator of gas with densities lower than a few thousands particles/cm^3 is the ratio of the [O III] lines at 52 and 88 μm. Higher density gas can be probed using line ratios with higher critical densities such as [S III] 33/19 μm and [Ne III] 36/15 μm.

4.1. [O III] diagnostic

The densities derived from the [O III] line ratio for the ISO sample of H II regions are in the range from $\sim$100 to 3000 cm^{-3} (see Table 5). No dependence of the density on galactocentric distance is found (see Fig. 4), in agreement with previous studies (e.g. Simpson et al. 1995b; Afflerbach et al. 1997).

The derived [O III] densities, $n_{\rm e}$([O III]), are compared to the rms densities, $n_{\rm e,rms}$, calculated from the radio continuum observations (see Table 2) in Fig. 5. In general, the rms densities are larger than the [O III] densities, except for three sources (IR 19207, IR 21270 and IR 22308), which are more extended (their radio sizes are 140, 120 and 90$''$, respectively) than the LWS aperture.

If the radio and ISO sample the same gas and there is no collisional de-excitation, $n_{\rm e}$([O III]) reflects the mean of the local density and must always be of the same order or greater than $n_{\rm e,rms}$, which is derived assuming that the emission is spread uniformly along the line of sight. The ratio of both densities is the filling factor, which has been found to be typically of the order of $\sim$0.1 for many H II regions (Copetti et al. 2000). The sources with $n_{\rm e,rms} < n_{\rm e}$([O III]) likely contain high density clumps embedded in a hot, low density gas from stellar winds. However, Fig. 5 shows that $n_{\rm e}$([O III]) is much too low for most of the sources. At the densities implied by the radio continuum observations, the [O III] line at 88 μm (with $n_{\rm crit} = 450$ cm^{-3}) is collisionally de-excited in the ultracompact core of the H II region. Considering that the real densities of these cores are probably even higher than our derived rms densities, even the [O III] line at 52 μm ($n_{\rm crit} = 3.1 \times 10^3$ cm^{-3}) could also well be collisionaly de-excited. Therefore, the density derived from the [O III] lines is likely representative of a dilute shell surrounding

Table 5. Electron densities derived from the [O III] 88/52 μm line ratio.

Source	$n_{\rm e}$([O III]) (cm^{-3})	Source	$n_{\rm e}$([O III]) (cm^{-3})
IR 02219	$2834\,^{+1225}_{-680}$	IR 18116	$753\,^{+224}_{-152}$
IR 10589	$645\,^{+194}_{-132}$	IR 18317	$1543\,^{+738}_{-397}$
IR 11143	$290\,^{+103}_{-71}$	IR 18434	$817\,^{+260}_{-171}$
IR 12063	$1335\,^{+454}_{-284}$	IR 18469	$146\,^{+65}_{-46}$
IR 12073	$962\,^{+295}_{-195}$	IR 18479	$836\,^{+268}_{-175}$
IR 12331	$623\,^{+181}_{-125}$	IR 18502	$1181\,^{+411}_{-257}$
IR 15384	$1224\,^{+390}_{-251}$	IR 19207	$485\,^{+152}_{-104}$
IR 15502	$452\,^{+178}_{-114}$	IR 19598	$484\,^{+154}_{-105}$
IR 16128	$891\,^{+271}_{-180}$	DR 21	$320\,^{+139}_{-90}$
IR 17160	$476\,^{+144}_{-100}$	IR 21190	$2882\,^{+1987}_{-871}$
IR 17221	$594\,^{+182}_{-124}$	IR 21270	$186\,^{+74}_{-52}$
IR 17279	$127\,^{+61}_{-44}$	IR 21306	$214\,^{+109}_{-70}$
Sgr C	$107\,^{+66}_{-45}$	IR 22308	$768\,^{+366}_{-207}$
IR 17455	$548\,^{+181}_{-121}$	IR 23030	$806\,^{+246}_{-164}$
IR 17591	$462\,^{+143}_{-99}$	IR 23133	<478
IR 18032	$512\,^{+274}_{-154}$		

the ultracompact core. This low density gas at high excitation (note that O^{++} is produced by ionizing photons with $h\nu > 35$ eV) could be produced by leakage of radiation from the core. Recent radio observations (Kurtz et al. 1999; Kim & Koo 2001) have shown that the presence of physically related envelopes around ultracompact H II regions is the usual case rather than the exception.

4.2. [S III] and [Ne III] diagnostics

The derivation of electron densities using the [S III] and [Ne III] line ratios from the ISO data yielded inconsistent results. Figure 6 compares the observed line ratios of these ions with their expected values for uniform electron densities between 10^2 and 10^6 cm^{-3}, plotted as a solid line. The assumed $T_{\rm e}$ of 7500 K has almost no effect on the plot. Meaningful [S III] and [Ne III] line ratios should lie below their expected values at low densities, but we see that almost all points for the [Ne III] line ratio, and many for [S III], lie above these limits by up to a factor of 3. This problem has also been recognized for the [Ne III] line ratio in some planetary nebula (Rubin et al. 2000). However, in that case the observed ratio is only 10% larger than what theory predicts for the low density limit. Possible causes of this discrepancy between observations and theory are:

Aperture The lines involved in both [S III] and [Ne III] ratios have been observed in different apertures ($14'' \times 27''$ and $20'' \times 33''$, respectively for the short and long wavelength lines). The black, large arrows in the bottom
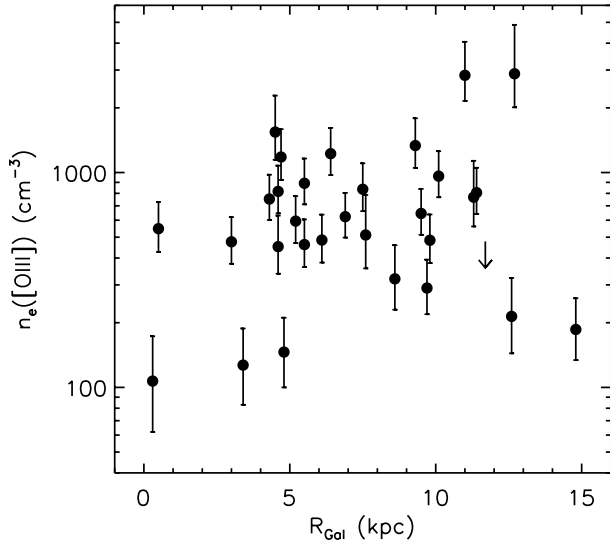
Fig. 4. Electron densities of the compact H II regions derived from the [O III] 88/52 μm line ratio plotted against $R_{\rm Gal}$. The arrow indicates an upper limit.
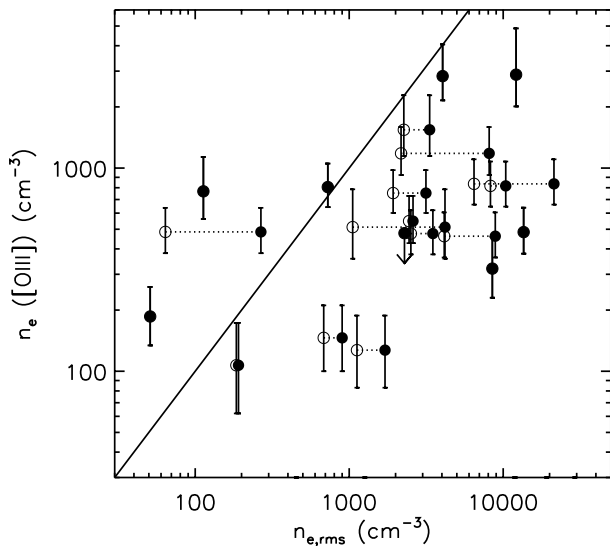

Fig. 5. Comparison between the electron densities of the compact H II regions derived from the [O III] 88/52 μm line ratio, $n_{\rm e}([{\rm O\,III}])$, and the radio continuum, $n_{\rm e,rms}$. The dotted lines join the $n_{\rm e,rms}$ as derived using both the near and far solar distances. The solid line represents the one-to-one relationship. The fact that $n_{\rm e}([{\rm O\,III}])$ is generally lower than $n_{\rm e,rms}$ shows that the [O III] lines are collisionally de-excited in the central regions of the objects, so that ISO LWS observes only a surrounding shell of low density gas.

right corner of Fig. 6 indicate the shift in both line ratios that might be caused by aperture effect if the emitting region is larger than the SWS band 4 ($20'' \times 33''$) and has an uniform brightness. Aperture effects may have affected the sources which cluster around a [S III] ratio of unity. Actually, this correction would bring these sources within the expected [S III] and [Ne III] ranges at densities of about 10^3–10^4 cm^{-3}, the rms density range. However, this

aperture correction is not large enough to bring the most-offending sources (IR 16128, IR 17160, IR 17279, IR 17591, IR 18469 and IR 19207), with a [S III] ratio $\sim$3, into the theoretical limits. Instead, these sources are undoubtedly off because only part of these sources were included in the SWS beam. Specifically, recent 6 cm ATCA maps of IR 16128, IR 17160 and IR 17279 (Martín-Hernández et al. 2002, in prep.) show that SWS was pointing at the edge of these sources and more of the source was included in the larger aperture of the longer wavelength lines than in that of the shorter wavelength lines. Likewise, radio maps of the sources IR 17591 (Garay et al. 1993), IR 18469 (Kurtz et al. 1994) and IR 19207 (Mehringer 1994) reveal complex structure – core halo or multiple components – part of which was not included in the short wavelength, smaller aperture.

Calibration The lines at the longest wavelengths, [S III] 33 and [Ne III] 36 μm, are located in the SWS band 4. Band 4 detectors suffer strongly from memory effects, are very sensitive to cosmic particle hits and their responsivity curve is still unsatisfactory and based on pre-flight ground based tests (see Paper I). Therefore, these lines are affected by large calibration errors (an official 1σ 25% calibration error is quoted in Paper I and used in Fig. 6). However, this calibration uncertainty is not enough to explain the discrepancy between the observed and the predicted line ratios.

Atomic parameters The most recent theoretical calculations (McLaughlin & Bell 2000) of the collisional strengths for the [Ne III] levels differ from earlier studies (Butler & Zeippen 1994) by only a few percent. Hence, we consider it unlikely that the observed factor 2–3 discrepancy in the [Ne III] line ratios of H II regions results from errors in the theoretical collisional strengths.

Extinction The lines involved in both [S III] and [Ne III] ratios suffer also from differential extinction. The color excesses between the [S III] lines and the [Ne III] lines are $E \simeq 0.15\,A_K$ and $E \simeq 0.10\,A_K$ (cf. Table 4), respectively. For the nominal $A_K \sim 2$ mag. derived from the H I recombination lines (cf. Table 3), these extinction corrections (indicated in Fig. 6 by the grey arrows in the bottom right corner) are, however, quite small.

We conclude that the present [S III] and [Ne III] line ratio observations are unreliable as density indicators largely due to aperture differences. The sources above mentioned (IR 16128, IR 17160, IR 17279, IR 17591, IR 18469 and IR 19207), together with IR 21270 and IR 21306, which, although not present in Fig. 6 are known to be mispointed (see Paper I), will be excluded from the analysis involving any SWS line. Moreover, the [S III] 33 and [Ne III] 36 μm lines will not be used in the data analysis.

The object IR 21190, identified in Fig. 6, is of special interest. It is a very compact H II region (and thus point-like for the SWS; see its spectrum in Fig. 8, Paper I, which does not present jumps between the different apertures) and has an $A_K = 0$ (see Table 3). Thus, it should
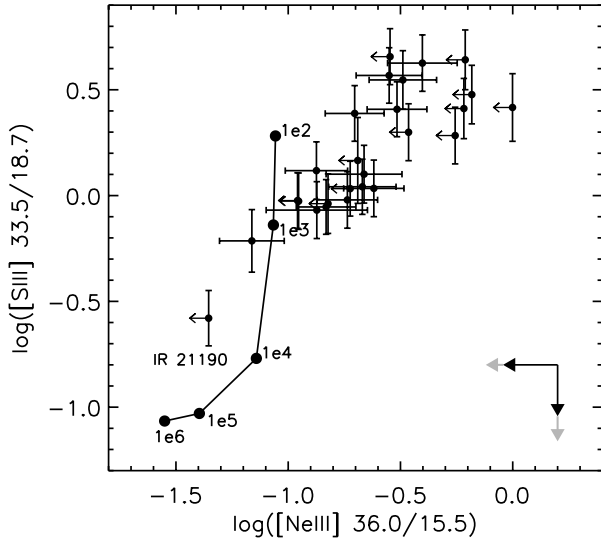
Fig. 6. Comparison between the observed line ratios [S III] 33/19 μm and [Ne III] 36/15 μm. Upper limits for the line ratios are indicated. The solid line represents the theoretical values of the [S III] and [Ne III] line ratios for the electron densities 10^2, 10^3, 10^4, 10^5 and 10^6 cm^{-3}. The large, black arrows in the bottom right corner indicate the shift ($\sim$0.23 in logarithmic scale) due to beam correction for an extended, uniform source. They are followed by short, grey arrows which indicate the extinction correction due to an $A_K = 2$ mag. The source IR 21190 is indicated (see text).

not be affected by aperture changes or extinction. Indeed, the [S III] and [Ne III] ratios for this source are well inside the theoretical limits. However, the densities derived from these two indicators ($n_e < 10^4$ cm^{-3} and $>10^5$ cm^{-3}, respectively for the [S III] and [Ne III] ratios) do not agree. IRAS 21190 presents a complex density morphology (Peeters et al. 2002, in prep.) and it is therefore not surprising that the tracer of lower density and lower ionization state material yields a lower density than the tracer of higher density and higher ionization state material.

5. Abundance determinations

5.1. Methodology

Ionic abundances can be determined from the measured strengths of the lines when a specific model for the structure of the H II region is assumed. The simplest model is to assume that the nebula is homogeneous with constant T_e and n_e. If one also assumes that all the line photons emitted in the nebula escape without absorption and therefore without causing further upward transitions, the calculation of the ionic abundances is straightforward (e.g. Rubin et al. 1988).

Considering two ions X^{+i} and Y^{+j}, the ratio of their ionic abundances is given by:

$$\frac{X^{+i}}{Y^{+j}} = \frac{F_{X^{+i}}/F_{Y^{+j}}}{\epsilon_{X^{+i}}/\epsilon_{Y^{+j}}}, \tag{10}$$

where $F_{X^{+i}}$ and $F_{Y^{+j}}$ are the fluxes corrected from extinction corresponding to any line produced by the ions X^{+i} and Y^{+j}, and $\epsilon_{X^{+i}}$ and $\epsilon_{Y^{+j}}$ are their respective emission coefficients. This equation assumes that the volume occupied by both ionic gases and the solid angles included in the fluxes are the same. Because the beam sizes of ISO differ significantly with wavelength (see Paper I), the distribution of the emission over the beam becomes important in determining abundances for some of the elements.

The emission coefficients depend on T_e, n_e and the relevant atomic parameters (transition probabilities, A, and collisional strengths, Ω). They are computed using a 5-level atom (or a 2-level atom for ions with a ^{2}P ground term) in statistical equilibrium (Kafatos & Lynch 1980). The references for the atomic parameters used in this paper are given in Table 1. Fortunately, the emissivities of the fine-structure lines show only a very slight dependence on T_e because these lines are emitted from levels with excitation energies much lower than the mean colliding electron energy. Thus, we will use an electron temperature of 7500 K, typical for galactic H II regions (Shaver et al. 1983; Afflerbach et al. 1996, 1997), to evaluate these emissivities. However, the dependence of the fine-structure emission coefficients on n_e is particularly important when the density of the emitting region is comparable to the critical density of the levels involved. It is illustrative to consider the n_e correction factor, $\delta(X^{+i+1}/X^{+i})_{n_e}$, needed to apply to the abundance ratio of sequential ionic ionization states (Ne^{++}/Ne$^+$, calculated from [Ne II] 12.8 and [Ne III] 15.5 μm, Ar^{++}/Ar$^+$, from [Ar II] 7.0 and [Ar III] 9.0 μm, S^{+3}/S^{++} from [S III] 18.7 and [S IV] 10.5 μm, and N^{++}/N$^+$, from [N II] 122 and [N III] 57 μm) when the respective line emissivities are evaluated in the low density limit (cf. Fig. 7). This correction factor is, basically, the quotient between the ratio of the respective emissivities evaluated at a density n_e and in the low density limit. Over most of our parameter space (ie. $n_e \lesssim 10^4$ cm^{-3}, cf. Fig. 5), Ne^{++}/Ne$^+$ and Ar^{++}/Ar$^+$ can be considered in the low density limit. The correction factor for S^{+3}/S^{++} is not larger than 1.35. N^{++}/N$^+$ can be overestimated by up to a factor of 3. However, the strong dependence of N^{++}/N$^+$ on n_e can be circumvented by the use of the LWS [O III] densities, which characterize the ionic gas in the same region where the nitrogen lines are produced.

To derive the ionic abundances with respect to hydrogen, one needs the H$^+$ emission associated with the nebula. These can be derived from a near-infrared H I recombination line, for instance Brα, which is detected in most of the sources, using Eq. (10) as follows:

$$\frac{X^{+i}}{H^+} = \frac{F_{X^{+i}}/F_{Br\alpha}}{\epsilon_{X^{+i}}/\epsilon_{Br\alpha}}. \tag{11}$$

The H I emission coefficients show a dependence on electron temperature that goes as $T_e^{-\alpha}$ ($\alpha = 1.23$ for Brα, Hummer & Storey 1987). The electron temperature in H II regions has been shown to increase with the galactocentric distance (Shaver et al. 1983; Afflerbach et al. 1996, 1997; Deharveng et al. 2000) from approximately 5000 K in the
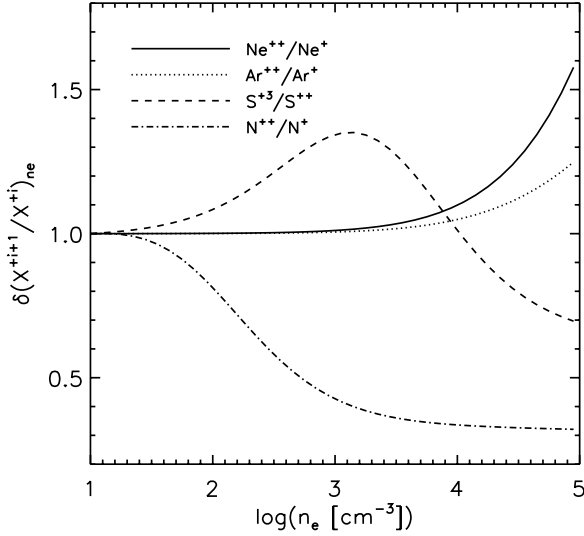
Fig. 7. The n_e correction factor $\delta(X^{+i+1}/X^{+i})_{n_e}$ needed to apply to the ionic ratio X^{+i+1}/X^{+i} when the line emission coefficients are evaluated in the low density limit is plotted as a function of n_e.
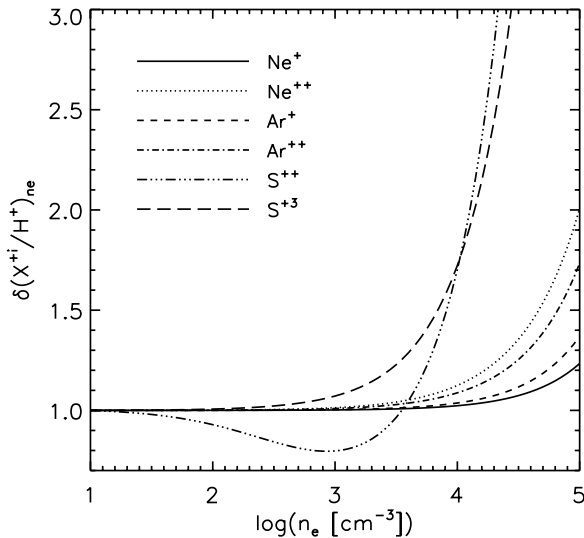

Fig. 8. The n_e correction factor $\delta(X^{+i}/H^+)_{n_e}$ needed to apply to the ionic abundance X^{+i}/H^+ when the line emission coefficients are evaluated in the low density limit is plotted as a function of n_e.

Galactic Center to 10 000 K at 15 kpc. Hence, if a single electron temperature of 7500 K is assumed, the Galactic T_e gradient will introduce a systematic bias in the abundance determinations. We can introduce a T_e correction factor $\delta(X^{+i}/H^+)_{T_e}$, defined as $(X^{+i}/H^+)_{T_e}/(X^{+i}/H^+)_{7500\,K} \approx (T_e/7500)^{-1.23}$. This correction factor goes from $\sim$1.6 at 5000 K to $\sim$0.7 at 10 000 K.

The H^+ emission can also be derived from optically thin, radio continuum observations. Combining Eqs. (9) and (11):

$$\frac{X^{+i}}{H^+} = 1.03 \times 10^{-14} T_e^{-0.35} \left(\frac{F_{X^{+i}}}{\epsilon_{X^{+i}}}\right) \left(\frac{\nu^{-0.1}}{S_\nu}\right) \left(\frac{n_e}{n_p}\right), (12)$$

where F_{X+i} is in units of $\mathrm{erg\,s^{-1}\,cm^{-2}}$, ϵ_{X+i} in $\mathrm{erg\,s^{-1}\,cm^3}$, T_e in K, ν in GHz and S_ν in Jy. The ratio of electrons to protons, n_e/n_p, differs from unity because of the contribution of singly ionized He to the total number of electrons. This can be included by using $n_e/n_p \approx 1 + N_{He^+}/N_{H^+} \approx 1.10$. As can be seen from equation 12, this method shows a small dependence on T_e and the assumption of a single $T_e = 7500$ K gives correction factors of the order of 15% at most.

The dependence on n_e of the fine-structure emission coefficients can also produce systematic uncertainties in the derived ionic abundances with respect to H^+. Figure 8 illustrates the case of the neon, argon and sulphur ionic abundances (calculated using the lines [Ne II] 12.8, [Ne III] 15.5, [Ar II] 7.0, [Ar III] 9.0, [S III] 18.7 and [S IV] 10.5 μm) and plots the n_e correction factor, $\delta(X^{+i}/H^+)_{n_e} \approx [\epsilon_{X+i}(n_e)/\epsilon_{X+i}(n_e \to 0)]^{-1}$, needed to apply when the low density limit is assumed. This correction becomes larger than 1 when $n_e > n_{crit}$. For the neon and argon abundances, this correction only becomes important for $n_e > 10^4$ cm^{-3}. More critical is the case of the sulphur abundances because of the lower critical densities of the [S III] 18.7 μm (10^4 cm^{-3}) and [S IV] 10.5 μm (3.7×10^4 cm^{-3}) lines. At densities around 10^4 cm^{-3}, the sulphur abundance will be underestimated by a factor of 2. Even more dramatic, although not shown in Fig. 8, is the case of N^+/H^+, N^{++}/H^+ and O^{++}/H^+. As in the case of N^{++}/N^+, their strong n_e dependence can be circumvented by the use of the LWS [O III] densities.

The total abundance of a given element is calculated by adding the contributions of the different ionic species of that element. However, ionization correction factors (ICFs) must be applied when some of the ionic species are not observed. The nebular abundances are then determined by:

$$\frac{X}{H} \simeq \sum_{i>0} \frac{X^{+i}}{H^+} = \mathrm{ICF}_{\mathrm{unobserved\ ions}} \times \sum_{\mathrm{observed}\ i} \frac{X^{+i}}{H^+}. \quad (13)$$

In the case of the ISO spectral data, all the elements except oxygen are observed in two ionization stages (see Fig. 1) and the ionization corrections will therefore be close to unity for Ar, Ne, S and N. In the case of oxygen, the abundance can only be derived by applying the ICF for the unseen O^+

5.2. Photoionization models

In order to evaluate in detail the dependence of the atomic fine-structure line flux ratios of the H II regions on the physical conditions (stellar and nebular properties), a set of photoionization models based on the code NEBU (Morisset & Pequignot 1996) was performed. For the stellar spectral energy distribution (SED), the CoStar atmosphere models of Schaerer & de Koter (1997) were used. These non-LTE stellar models include the effects of stellar wind and line blanketing, important for massive stars. A total of 26 CoStar models are available with effective

temperatures ranging from 22 to 55 kK and luminosities from 1.5×10^{38} to $8 \times 10^{39}\,\mathrm{erg\,s^{-1}}$. For each stellar atmosphere model, a series of photoionization models was build for nebular densities of 3×10^2, 10^3, 3×10^3, 10^4, 3×10^4 and $10^5\,\mathrm{cm^{-3}}$, which cover the density range probed by the atomic fine-structure lines detected in the ISO spectra. The nebulae are assumed to be spherically symmetric. The nebular abundances are solar (Grevesse & Sauval 1998), the distance between the star and the nebula is taken to be 3×10^{17} cm and the filling factor of the gas is supposed to be unity. In total, 156 nebular models were calculated spanning a wide range in stellar properties (one order of magnitude in luminosity) and nebular densities (two orders of magnitude), corresponding to a range in the ionization parameter of more than 3 orders of magnitude. This large range in ionization parameter combined with the effective stellar temperatures is likely to describe the physical conditions of the sample of H II regions. Since the main results deal with the predictions of line flux ratios, the distances to the objects are not relevant. A detailed comparison of the predictions of such a model with the ISO spectrum of the compact H II region IRAS 18434−0242 (G29.96−0.02) is given in Morisset et al. (2001) – hereafter Paper III.

6. Ionization state

Any two successive stages of ionization i and $i{+}1$ of a given element can be used as a measure of the state of ionization of the nebula. The line ratios [Ar III]/[Ar II] 9.0/7.0, [N III]/[N II] 57.3/121.7, [S IV]/[S III] 10.5/18.7 and [Ne III]/[Ne II] 15.5/12.8 μm can be used to determine (cf. equation 10) the relative ionic abundance ratios $\mathrm{Ar^{++}/Ar^+}$, $\mathrm{N^{++}/N^+}$, $\mathrm{S^{+3}/S^{++}}$ and $\mathrm{Ne^{++}/Ne^+}$, respectively. A single $T_e = 7500\,\mathrm{K}$ and the low density limit (except for $\mathrm{N^{++}/N^+}$, which was evaluated using the [O III] densities calculated in Sect. 4) are assumed in the derivation. The results are presented in Table 6, assuming no correction for beam differences or for differential extinction. As mentioned in Sect. 5, the low density limit is valid for $\mathrm{Ne^{++}/Ne^+}$ and $\mathrm{Ar^{++}/Ar^+}$ over the range of the derived $n_e([\mathrm{O\,III}])$ and $n_{e,\mathrm{rms}}$ ($n_e \leq 10^4\,\mathrm{cm^{-3}}$), while $\mathrm{S^{+3}/S^{++}}$ may be affected by up to a 35% uncertainty. The errors listed in Table 6 stem from the direct propagation of the line flux uncertainties (the $\mathrm{N^{++}/N^+}$ analysis includes also the uncertainties in the [O III] density). [Ne III]/[Ne II] is not affected by calibration errors because the lines involved in the ratio are measured in the same spectral band (see Paper I), resulting in smaller errors.

Successive stages of ionization X^{+i} and X^{+i+1} of a given element indicate the state of ionization of the nebula, which depends only, in first approximation, on the ionization parameter, U, and the hardness of the ionizing radiation (Vílchez & Pagel 1988):

$$\frac{X^{+i+1}}{X^{+i}} \propto U \frac{\int_{\nu(X^{+i})}^{\infty} \frac{J_\nu}{h\nu}\mathrm{d}\nu}{\int_{13.6\,\mathrm{eV}}^{\infty} \frac{J_\nu}{h\nu}\mathrm{d}\nu} \ , \tag{14}$$

Table 6. Ionic abundances X^{+i+1}/X^{+i} for argon, nitrogen, sulphur and neon derived in the low density limit (except for $\mathrm{N^{++}/N^+}$, which was evaluated using the [O III] densities calculated in Sect. 4).

Source	$\mathrm{Ar^{++}/Ar^+}$	$\mathrm{N^{++}/N^+}$	$\mathrm{S^{+3}/S^{++}}$	$\mathrm{Ne^{++}/Ne^+}$
IR 01045	–	–	<0.07	0.28 ± 0.07
IR 02219	5.9 ± 0.6	>0.8	0.13 ± 0.02	1.07 ± 0.06
IR 10589	0.90 ± 0.10	0.4 ± 0.1	0.018 ± 0.004	0.13 ± 0.01
IR 11143	>14	3 ± 1	0.21 ± 0.04	2.0 ± 0.2
IR 12063	4.6 ± 0.6	>1	0.15 ± 0.03	0.88 ± 0.06
IR 12073	15 ± 5	>3	0.34 ± 0.06	2.7 ± 0.3
IR 12331	2.1 ± 0.3	0.8 ± 0.2	0.027 ± 0.005	0.32 ± 0.02
IR 15384	0.7 ± 0.1	0.5 ± 0.2	0.020 ± 0.004	0.14 ± 0.02
IR 15502	0.24 ± 0.04	0.5 ± 0.2	0.009 ± 0.002	0.11 ± 0.02
IR 16128	–	0.7 ± 0.2	–	–
IR 17160	–	0.31 ± 0.09	–	–
IR 17221	0.28 ± 0.04	0.16 ± 0.05	0.004 ± 0.001	0.018 ± 0.004
IR 17279	–	0.24 ± 0.06	–	–
Sgr C	<0.04	0.10 ± 0.03	<0.01	<0.02
IR 17455	0.66 ± 0.07	0.6 ± 0.2	0.016 ± 0.003	0.20 ± 0.01
IR 17591	–	0.4 ± 0.1	–	–
IR 18032	0.14 ± 0.02	0.19 ± 0.08	<0.003	<0.01
IR 18116	0.12 ± 0.01	0.23 ± 0.07	<0.002	0.033 ± 0.008
IR 18317	0.22 ± 0.02	0.10 ± 0.04	0.003 ± 0.001	0.029 ± 0.002
IR 18434	0.56 ± 0.08	0.4 ± 0.1	0.018 ± 0.004	0.12 ± 0.01
IR 18469	–	0.4 ± 0.1	–	–
IR 18479	<0.1	>0.2	<0.01	0.21 ± 0.03
IR 18502	0.38 ± 0.06	>0.4	0.011 ± 0.003	0.100 ± 0.008
IR 19207	–	1.3 ± 0.4	–	–
IR 19442	<0.05	–	<0.03	<0.01
IR 19598	1.4 ± 0.2	>0.4	0.09 ± 0.02	1.04 ± 0.04
DR 21	0.12 ± 0.03	–	<0.009	0.12 ± 0.05
IR 21190	2.9 ± 0.4	–	0.06 ± 0.01	0.43 ± 0.02
IR 21270	–	>0.7	–	–
IR 22308	0.23 ± 0.08	>0.2	<0.008	<0.02
IR 23030	2.0 ± 0.3	0.5 ± 0.2	0.016 ± 0.003	0.063 ± 0.003
IR 23133	0.25 ± 0.03	–	0.004 ± 0.001	<0.01

where J_ν is the mean intensity of the radiation. Therefore, a ratio X^{+i+1}/X^{+i} is, to first order and for a given U, proportional to the relative number of photons able to ionize X^{+i}, ie. above $\nu(X^{+i})$, as compared to that of Lyman continuum photons (above 13.6 eV). Hence, $\mathrm{Ar^{++}/Ar^+}$, $\mathrm{N^{++}/N^+}$, $\mathrm{S^{+3}/S^{++}}$ and $\mathrm{Ne^{++}/Ne^+}$ probe the hardness of the stellar radiation between 13.6 eV and 28, 30, 35 and 41 eV, respectively (see Fig. 1).

The behaviour of these "hardness" indicators with galactocentric distance (cf. Fig. 9) shows that the highest ionized H II regions are located at the highest galactocentric distances. Assuming no systematic variations of U with R_{Gal}, Fig. 9 indicates, consequently, a hardening of the radiation field towards large galactocentric distances.

A ratio $(X^{i+1}/X^{+i})/(Y^{i+1}/Y^{+i})$ involving two different elements X and Y measures to first order, according to Eq. (14), the relative number of ionizing photons in the respective ionizing continua (e.g. Vílchez & Pagel 1988), ie. above $\nu(X^{+i})$ and $\nu(Y^{+i})$, respectively. Figure 10 shows the correlations between the 4 "hardness" indicators, ie. $\log(\mathrm{Ar^{++}/Ar^+})$ vs. $\log(\mathrm{N^{++}/N^+})$, $\log(\mathrm{N^{++}/N^+})$ vs. $\log(\mathrm{S^{+3}/S^{++}})$, $\log(\mathrm{S^{+3}/S^{++}})$ vs. $\log(\mathrm{Ne^{++}/Ne^+})$ and $\log(\mathrm{Ne^{++}/Ne^+})$ vs. $\log(\mathrm{Ar^{++}/Ar^+})$. The arrows indicate the extinction correction to be applied if the "standard"

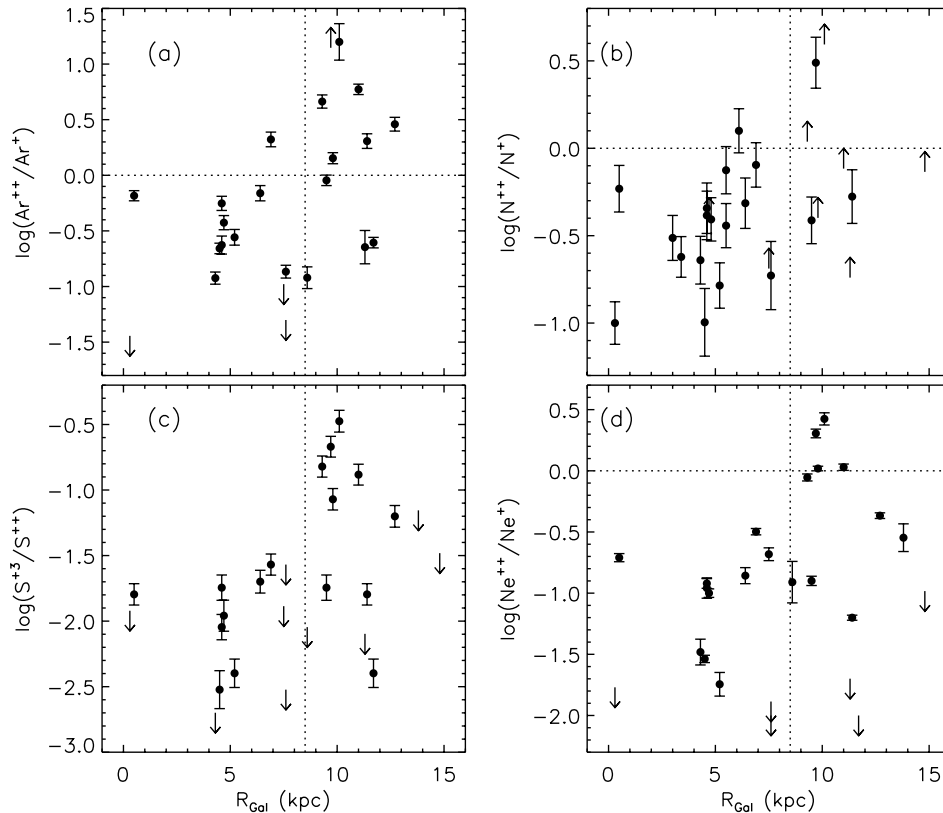**Fig. 9.** The spectral "hardness" indicators Ar^{++}/Ar^+, N^{++}/N^+, S^{+3}/S^{++} and Ne^{++}/Ne^+ plotted against R_{Gal}. The dotted lines are intended only to guide the eye: the vertical line indicates the solar position at 8.5 kpc and the horizontal one indicates when $X^{+i+1}/X^{+i} = 1$. The upper and lower limits are indicated by down and upwards arrows, respectively.

extinction law (see Sect. 3.1) is assumed. The extinction correction for the neon and nitrogen line ratios is negligible. The dotted line in every panel represents a straight line fit to the data and is a fairly good representation of the data behaviour. The slopes obtained from a least squares fit are very close to one: 1.2 ± 0.3, 0.76 ± 0.07, 0.93 ± 0.06 and 0.8 ± 0.1, respectively for panels a, b, c and d. Because these ionic pairs probe the ionizing energies up to 41 eV, Fig. 10 shows that the hardening of the radiation field affects equally the full range of the ionizing spectra.

Photoionization models, however, show an additional dependence of $(X^{+i+1}/X^{+i})/(Y^{+i+1}/Y^{+i})$ on U (Stasińska & Schaerer 1997, Paper III) rendering the interpretation more complex and probably producing part of the scatter in Figs. 9 and 10. The set of photoionization models described in Sect. 5.2 allows us to study the influence of the ionization parameter U and the stellar effective temperature T_{eff} (ie. the shape of the ionizing spectrum) on the ionization state of the gas, traced by any of the ratios X^{+i+1}/X^{+i}, for instance Ne^{++}/Ne^+. The variation of Ne^{++}/Ne^+ is shown as a function of T_{eff} in Fig. 11. For a given stellar atmosphere model or T_{eff}, this ratio decreases with increasing electron density. The observed Ne^{++}/Ne^+ ranges from ~ 0.01 to 3, a range predicted by the models for values of T_{eff} between 31 and 38 kK (Fig. 11). Similar variations are predicted for the other ionization ratios (N^{++}/N^+, Ar^{++}/Ar^+ and S^{+3}/S^{++}). Changing U at a given T_{eff} (by changing the stellar luminosity and/or the gas density) can change Ne^{++}/Ne^+ by a factor of 10 or

more. An estimate of the T_{eff} of the ionizing star is therefore only possible if robust constraints on U are available. A detailed study of the relations between the ionization diagnostics and the stellar atmosphere models is postponed to a future paper (Morisset et al. in prep.).

However, as tracers of the ionization state, the ionic abundance ratios X^{+i+1}/X^{+i} are sensitive indicators of the ionization correction factors. Figure 12 shows the ICFs for N, O, Ne, S and Ar derived from the grid of photoionization models as a function of Ne^{++}/Ne^+. The scatter in the calculated ionization correction factors is low, indicating that the use of the ionic abundance ratios X^{+i+1}/X^{+i} to constrain the ICFs is a robust method. In other words, even if U and the SED of the ionizing star are poorly known, the knowledge of the ionization state of the gas through the ionization ratios is enough to determine reliable ICFs. This conclusion does not strongly depend on the stellar atmosphere models as shown by comparing the results of a photoionization code using other atmosphere models (e.g. CMFGEN – Bourret, private communication).

The observed values of the ionization ratios can therefore be used to correct the elemental abundances for the unseen ions. As shown in Fig. 12, the effects are rather small, except for oxygen. The effect on the Ne abundance is negligible. In the case of sulphur, the abundance is always underestimated by typically $\sim 15\%$. For high ionization conditions, the abundances of N and Ar can be underestimated by up to 10 and 30%, respectively, because of the missing N^{+3} and Ar^{+3}. For O, only O^{++} is available
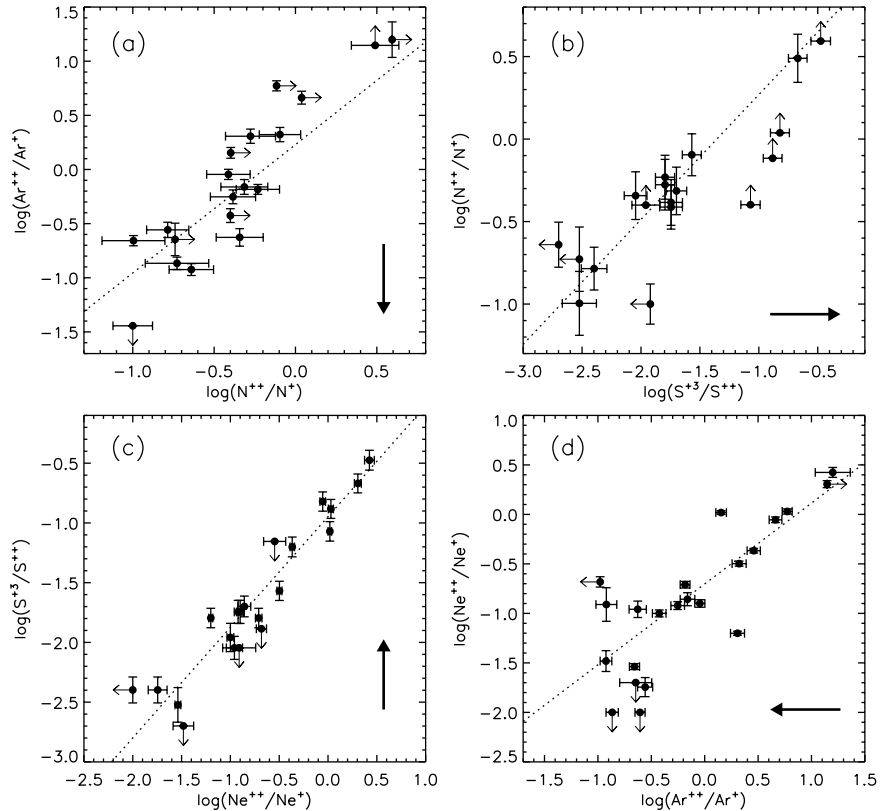
Fig. 10. Correlations between the ionic abundance ratios tracing the degree of ionization of the compact H II regions: **a)** Ar^{++}/Ar$^+$ vs. N^{++}/N$^+$, **b)** N^{++}/N$^+$ vs. S^{+3}/S^{++} **c)** S^{+3}/S^{++} vs. Ne^{++}/Ne$^+$ and **d)** Ne^{++}/Ne$^+$ vs. Ar^{++}/Ar$^+$. Upper/lower limits are indicated by short arrows. The long arrows indicate the direction of extinction correction. If using the "standard" extinction quoted in Table 4, the extinction corrections to apply are: **a)** 0.12×A_K, **b)** 0.08×A_K, **c)** 0.08×A_K and **d)** 0.12×A_K.

and thus, we are missing the low ionization state O$^+$. The ICF for O is very large, between 1.5 and 100.

7. Abundances

7.1. N^{++}/O^{++} and N/O

The N^{++}/O^{++} abundance ratio is straightforward to derive from equation 10 using the [N III] 57 μm and [O III] 52+88 μm line fluxes together with the densities derived from the [O III] 88/52 line ratio (Table 5), which are well adapted because both the N and O lines are emitted by low density gas. All three lines are observed with LWS and consequently, beam differences and differential extinction are negligible. Finally, the use of both [O III] lines minimizes considerably the dependence of the ionic abundance on n_e. The resulting N^{++}/O^{++} ionic abundance ratios are listed in Table 7 (the quoted uncertainties come from the error propagation of the line fluxes). The ionic abundance ratio N^{++}/O^{++} is found to decrease with galactocentric distance (Fig. 13).

The significance of N^{++}/O^{++} and its dependence on R_{Gal} has been discussed in detail in previous studies (e.g. Rubin et al. 1988,and references therein). N^{++}/O^{++} is a function of both the ionization state of the nebula (the ionization potentials of N$^+$ and O$^+$ are 29.6 and 35.1 eV, respectively) as well as of abundance, and one has to disentangle their effects to derive the N/O elemental abundance ratio. Figure 14 presents the correlation between N^{++}/O^{++} and Ne^{++}/Ne$^+$ (note that the spectral "hardness" indicators are inter-correlated and thus, they all
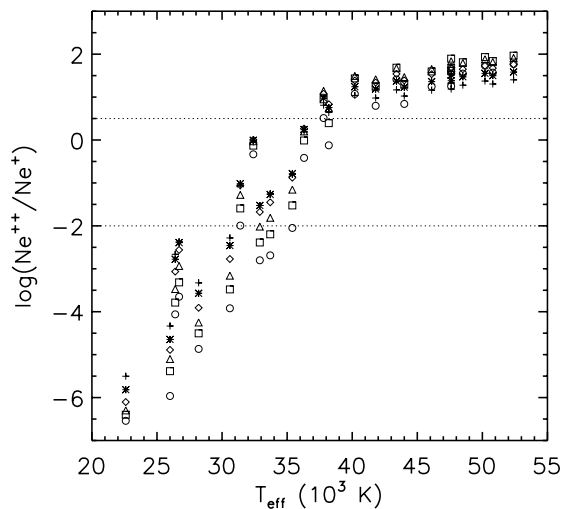

Fig. 11. Model predictions for Ne^{++}/Ne$^+$ as a function of stellar effective temperature (T_{eff}) and nebular density. The densities are indicated by various symbols: the plus sign, star, diamond, triangle, square and circle correspond to densities of 3×10^2, 10^3, 3×10^3, 10^4, 3×10^4 and 10^5 cm^{-3}, respectively. The observed range for Ne^{++}/Ne$^+$ ($\sim$0.01 to 3) in the ISO sample of H II regions is delineated by the dotted horizontal lines.

correlate with N^{++}/O^{++}). As can be seen in Figs. 13 and 14, N^{++}/O^{++} is inversely proportional to the degree of ionization (ie. low ionized nebulae have high N^{++}/O^{++} ionic abundances) and this dependence is connected to the location in the Galaxy (ie. nebulae with high N^{++}/O^{++} are preferentially located in the inner Galaxy). For these inner nebulae, N$^+$ and O$^+$ are probably the dominant

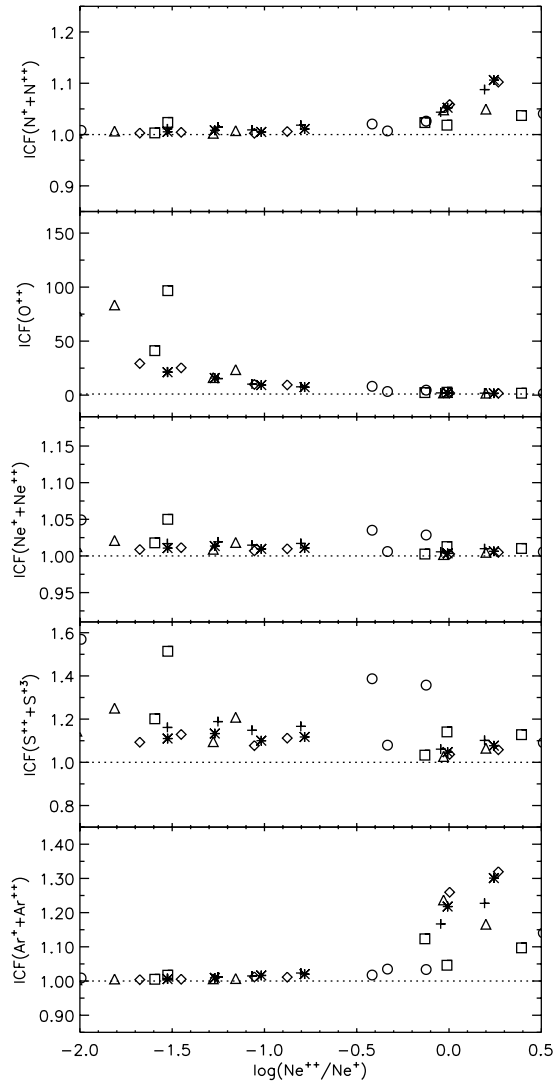**Fig. 12.** Model predictions for the ionization correction factors (ICFs) for N, O, Ne, S and Ar. The ICFs are plotted against Ne^{++}/Ne^+, which traces the ionization state. The dotted line indicates an ICF equal to one. The densities are indicated by various symbols: 3×10^2 cm^{-3} (plus signs), 10^3 cm^{-3} (stars), 3×10^3 cm^{-3} (diamonds), 10^4 cm^{-3} (triangles), 3×10^4 cm^{-3} (squares) and 10^5 cm^{-3} (circles).

ionic species over N^{++} and O^{++} and therefore, the ionization correction needed to get N/O from N^{++}/O^{++} could be rather large (N^{++}/O^{++} will be then overestimating N/O). In contrast, N^{++}/O^{++} must be close to N/O for the nebulae in the outer Galaxy.

The predictions of the photoionization models are useful to quantify the effects of ionization conditions on N^{++}/O^{++}. In particular, one can estimate the ionization correction factor which has to be applied by using one of the ionization diagnostic X^{+i+1}/X^{+i}. Based on the model results, an empirical method can be determined to derive the elemental abundance ratio N/O from the observed

Table 7. The ionic abundance ratio N^{++}/O^{++} as derived from the LWS fine-structure lines [N III] 57 μm and [O III] 52+88 μm.

Source	N^{++}/O^{++}	Source	N^{++}/O^{++}
IR 02219	0.16 ± 0.04	IR 18032	0.6 ± 0.1
IR 10589	0.24 ± 0.04	IR 18116	0.50 ± 0.08
IR 11143	0.14 ± 0.02	IR 18317	0.8 ± 0.1
IR 12063	0.18 ± 0.03	IR 18434	0.49 ± 0.07
IR 12073	0.13 ± 0.02	IR 18469	0.43 ± 0.07
IR 12331	0.30 ± 0.04	IR 18479	0.15 ± 0.04
IR 15384	0.41 ± 0.06	IR 18502	0.39 ± 0.07
IR 15502	0.47 ± 0.08	IR 19207	0.24 ± 0.04
IR 16128	0.38 ± 0.06	IR 19598	0.10 ± 0.02
IR 17160	0.50 ± 0.07	DR 21	< 0.21
IR 17221	0.7 ± 0.1	IR 21190	< 0.33
IR 17279	0.7 ± 0.1	IR 21270	0.17 ± 0.03
Sgr C	0.7 ± 0.1	IR 21306	< 0.13
IR 17455	0.44 ± 0.07	IR 22566	0.2 ± 0.1
IR 17591	0.12 ± 0.02	IR 23030	0.33 ± 0.05
IR 18032	0.6 ± 0.1		

[N III] and [O III] line fluxes. The N/O abundance ratio can be expressed as follows:

$$\frac{N}{O} = \frac{[N III]}{\Sigma[O III]} \times \frac{N^{++}/O^{++}}{[N III]/\Sigma[O III]} \times \frac{N/O}{N^{++}/O^{++}} , \qquad (15)$$

where the first term on the right side is the ratio of the [N III] and [O III] line fluxes, the second term is the ratio of the emissivities of these lines (taking into account the density effect leading to collisional de-excitation) and the third term is the ratio of the ICFs which have to be applied to N and O. $\Sigma[O III]$ is the sum of the two [O III] lines, ie. [O III] 52+88 μm.

The second and third member of the Eq. (15) can be empirically determined by the use of appropriate observables and the grid of models leading to the following relation:

$$\frac{N}{O} = \frac{[N III]}{\Sigma[O III]} \times \left(1.07r[O III]^{-0.29}\right)$$
$$\times \left(0.95 + 0.27\log\frac{[Ne III]}{[Ne II]}\right), \qquad (16)$$

where $r[O III]$ is the ratio [O III] 88/52 μm. The density correction via $r[O III]$, which transforms $[N III]/\Sigma[O III]$ into N^{++}/O^{++}, yields N^{++}/O^{++} ratios on average 10% lower than the N^{++}/O^{++} derived from Eq. (10), mainly due to slight differences between the atomic constants used in the code NEBU and the ones used in this work.

The photoionization model predictions of these successive ratios are shown in Fig. 15 as a function of degree of ionization (as measured by the ionic abundance ratio Ne^{++}/Ne^+): the line flux ratio $[N III]/\Sigma[O III]$ (plus signs), the ionic abundance ratio N^{++}/O^{++} (diamonds) and the elemental abundance ratio N/O after correcting for the
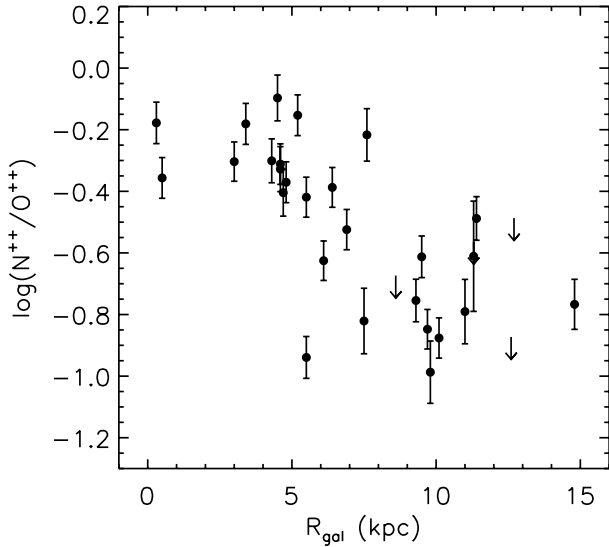
Fig. 13. Plot of the ionic abundance ratio N^{++}/O^{++} versus the galactocentric distance R_{Gal}. The upper limits are denoted by downwards arrows.

density and the unseen ions (stars). The dotted horizontal line indicates the input value of N/O of the model, ie. the solar ratio of 0.123 (Grevesse & Sauval 1998). As can be seen, when no ICF corrections are applied, the N^{++}/O^{++} ratio overestimates the N/O abundance ratio for low ionization conditions and slightly underestimates the N/O ratio for high ionization conditions. Finally, the results for the N/O abundance ratio after correcting for the density and the ICF dependence (stars in Fig. 15) agree very well with the input solar value of 0.123.

Equation (16) provides a useful empirical law to derive the N/O abundance ratio from the observed [O III], [N III] and neon line fluxes. Any deviation from the solar N/O abundance after applying this law to the observed [N III]/Σ[O III] indicates intrinsic variations in the N/O abundance ratio. Similar empirical laws can be derived for the [Ar III]/[Ar II] and [S IV]/[S III] ionization diagnostics. However, we prefer the method based on the neon lines, whose ratio is hardly affected by differential extinction and aperture differences. Note that the [N III]/[N II] has an extra dependence on density and is, therefore, less appropriate.

Figure 16 shows the N/O abundance ratio as a function of galactocentric distance after applying the corrections described above by using the neon lines. Note that there are only 25 sources for which the corrections could be applied. Whereas the slope of the variation is not as steep as that for N^{++}/O^{++} (see Fig. 13), a gradient of N/O with galactocentric distance is clearly present in the sense of a decreasing ratio with R_{Gal}:

$$\log\frac{N}{O} = (-0.23 \pm 0.07) - (0.056 \pm 0.009)R_{\mathrm{Gal}}. \quad (17)$$

The correlation coefficient of the least square fit is $r = -0.80$. This Galactic N/O gradient is consistent with previous studies of H II regions (Simpson et al. 1995b) and B stars (Smartt et al. 2001).
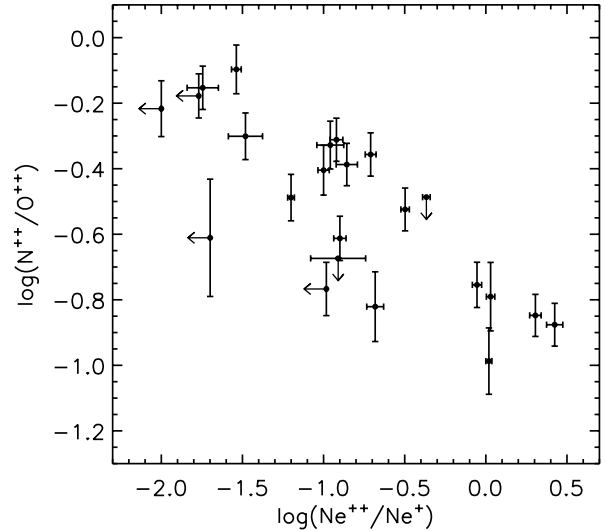

Fig. 14. Plot of N^{++}/O^{++} versus Ne^{++}/Ne^{+}, a degree of ionization indicator.
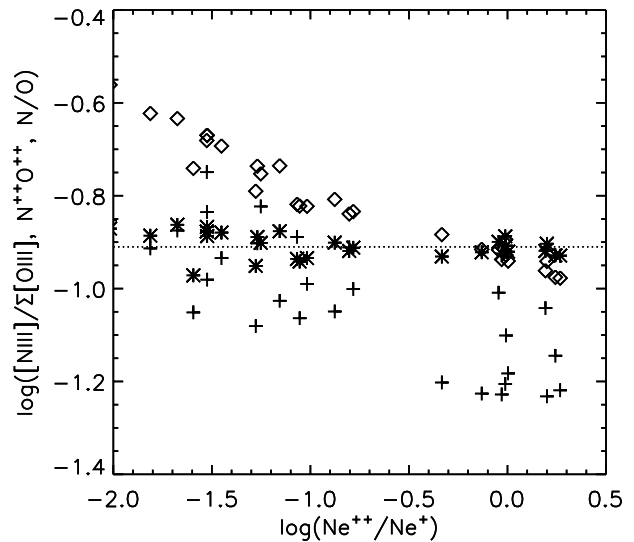

Fig. 15. Model predictions for the variation of [N III]/Σ[O III] (plus signs) as a function of the ionization diagnostic $Ne^{++}/Ne^{+} \propto$ [Ne III]/[Ne II]. The horizontal line indicates the input value of N/O of the model, ie. the solar ratio of 0.123. The ionic abundance ratios N^{++}/O^{++} (after correcting the line fluxes for the collisional de-excitation) are shown as diamonds. The N/O elemental abundance ratios (after correcting for the density and the unseen ions) are shown as stars – see text.

7.2. N/H and O^{++}/H^{+}

Because of the large difference between the SWS and LWS apertures and the fact that many sources are more extended than the SWS aperture, the hydrogen line flux corresponding to the gas where the nitrogen and oxygen lines are formed will be underestimated if a SWS H I recombination line is used. Thus, the resulting abundances of N and O will be overestimated. Hence, the radio continuum measurements are thought to be more appropriate to evaluate H^{+} and Eq. (12) is used to calculate N^{+}/H^{+}, N^{++}/H^{+} and O^{++}/H^{+} via the lines [N II] 122,
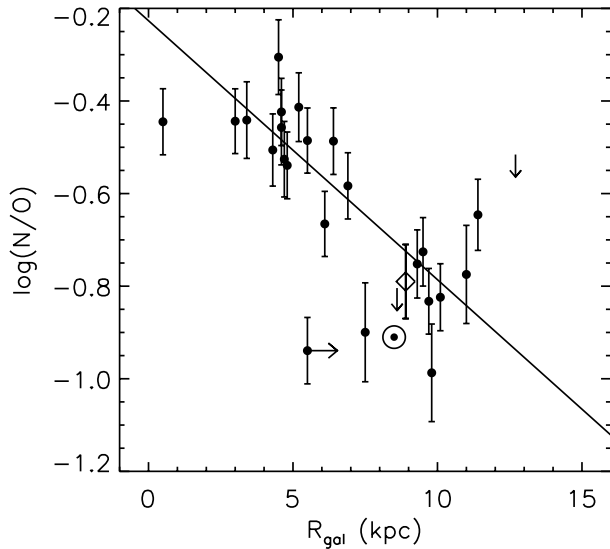
Fig. 16. Plot of the elemental abundance ratio N/O versus galactocentric distance R_{Gal} as derived from the N^{++}/O^{++} ratio – see text. The upper limits are denoted by downwards arrows.

Table 8. Ionic and total abundances derived from the LWS fine-structure lines. These abundances are very uncertain because of the possible mismatch between the gas observed by LWS and the radio emission used to derive H^+ (see Sect. 7.2).

Source	N^+/H^+ $\times 10^{-4}$	N^{++}/H^+ $\times 10^{-4}$	N/H $\times 10^{-4}$	O^{++}/H^+ $\times 10^{-4}$
IR 02219	<0.3	0.2 ± 0.1	<0.5	1.4 ± 0.6
IR 17160	1.5 ± 0.6	0.5 ± 0.2	2.0 ± 0.8	0.9 ± 0.3
IR 17279	9. ± 4.	2.0 ± 0.6	11. ± 4.	3.0 ± 0.9
IR 17455	1.3 ± 0.6	0.8 ± 0.3	2.1 ± 0.8	1.7 ± 0.6
IR 17591	0.3 ± 0.1	0.12 ± 0.04	0.5 ± 0.2	1.0 ± 0.3
IR 18032	1.7 ± 0.9	0.3 ± 0.1	2. ± 1.	0.5 ± 0.2
IR 18116	0.5 ± 0.2	0.11 ± 0.04	0.6 ± 0.2	0.21 ± 0.07
IR 18317	4. ± 2.	0.4 ± 0.2	5. ± 2.	0.5 ± 0.2
IR 18434	1.3 ± 0.6	0.5 ± 0.2	1.9 ± 0.8	1.1 ± 0.4
IR 18469	7. ± 3.	2.5 ± 0.8	9. ± 4.	6. ± 2.
IR 18479	<0.3	0.07 ± 0.03	<0.4	0.4 ± 0.2
IR 18502	<0.5	0.20 ± 0.08	<0.7	0.5 ± 0.2
IR 19598	<0.1	0.05 ± 0.02	<0.2	0.5 ± 0.2
DR 21	<0.04	<0.009	–	0.04 ± 0.01
IR 21190	<0.7	<0.2	–	0.6 ± 0.3
IR 23030	0.3 ± 0.1	0.16 ± 0.06	0.5 ± 0.2	0.5 ± 0.2

[N III] 57 and [O III] 52+88 μm. The radio flux densities from Table 2 are used and the sources which are more extended than the LWS aperture (Sgr C, IR 19207, IR 21270 and IR 22308) are excluded. [O III] densities (cf. Table 5) are used to evaluate the line emissivities involved.

For nitrogen, both ions N^+ and N^{++} are measured. Figure 9 shows that N^+ is the dominant species over N^{++} and therefore, N^{+3} is not expected to contribute significantly to the total abundance of nitrogen. Indeed, the grid of photoionization models (cf. Fig. 12) shows that the contribution of N^{+3} for the highest ionized sources is only at the 10% level. Hence, the total nitrogen abundance N/H is calculated by adding the ionic abundances N^+/H^+ and N^{++}/H^+. The calculated N^+/H^+, N^{++}/H^+ and N/H are given in Table 8. Figure 17a represents N/H versus R_{Gal}.
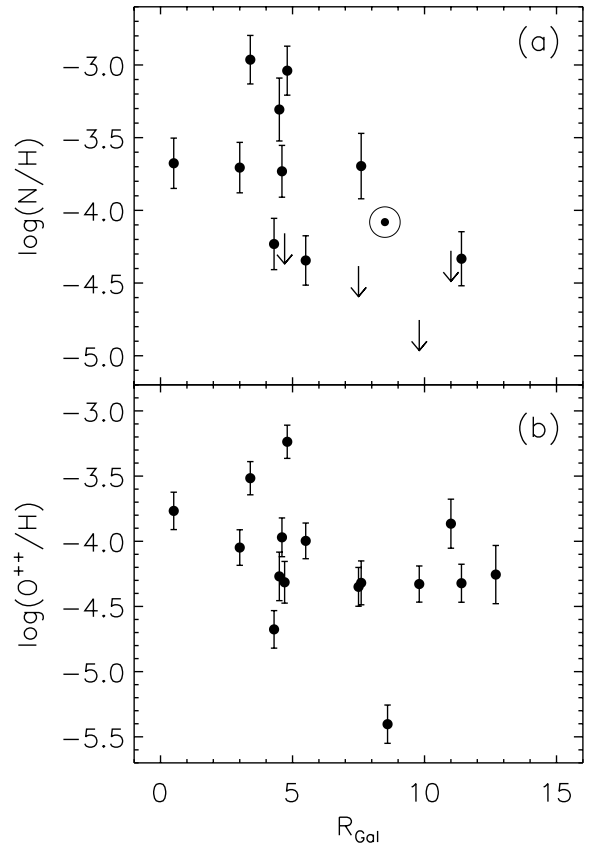

Fig. 17. a) N/H and **b)** O^{++}/H^+ as a function of R_{Gal}. The solar nitrogen abundance (Grevesse & Sauval 1998) is indicated by the symbol $\odot$.

An attempt to fit a straight line was made, but no statistically significant fit was possible because of the few points and the large scatter. We note that sources in the inner 5 kpc have supersolar nitrogen abundances, in agreement with determinations using B stars (e.g. Smartt et al. 2001).

For oxygen, only O^{++} is available and thus, we are missing O^+. We have used the grid of photoionization models to estimate the effect of the missing O^+ abundance. These models show that the ionization correction factor is very large, between 1.5 and 100 depending on the degree of ionization (cf. Fig. 12). Therefore, the derived O^{++}/H^+ listed in Table 8 can only be interpreted as a lower limit for the total O/H abundance. Figure 17b plots O^{++}/H^+ versus R_{Gal}. Clearly, the derived O^{++}/H^+ abundances are much lower than the solar $\log(\mathrm{O}/\mathrm{H}) = -3.2$ (Grevesse & Sauval 1998).

A note of caution must be brought concerning the nitrogen and oxygen abundances. In most cases, the ISO [O III] 88/52 μm line ratio give densities which are far below those required to produce the ultracompact H II emission observed at radio wavelengths ($n_{e,rms}$) (see Fig. 5). This suggests that the ultracompact H II regions are surrounded by a tenuous shell of O^{++} (and probably also N^{++}). If this is the case, both N and O^{++} abundances will not be the true nebular abundances as the

H^+ emission associated with the shell will not be the one given by the radio observations.

7.3. Ne/H, S/H and Ar/H

Despite the inherent uncertainty associated with the H I recombination line method concerning T_e (cf. Sect. 5), we will use the Brα line fluxes observed with ISO/SWS in analyzing all the SWS fine-structure lines of neon, sulphur and argon because the beams are well matched. As the lines of [Ne II] 12.8 and [Ne III] 15.5, [S III] 18.7 and [S IV] 10.5, and [Ar II] 7.0 and [Ar III] 9.0, used to determine the abundances of neon, sulphur and argon, respectively, are observed by a beam comparable to Brα, the use of Eq. (11) is straightforward. The fine-structure lines and H I recombination line emissivities involved in the calculation were evaluated in the low density limit and considering a single $T_e = 7500$ K. The lines in the SWS band 4, [S III] 33.4 and [Ne III] 36.0 μm, which are observed in a larger aperture and are affected by large calibration uncertainties, are not included in the determination (see discussion in Sect. 4).

The absolute abundances for neon, sulphur and argon were calculated adding the contribution from the different ionization stages available:

$$\frac{Ne}{H} = \frac{Ne^+}{H^+} + \frac{Ne^{++}}{H^+} \ ; \tag{18}$$

$$\frac{S}{H} = \frac{S^{++}}{H^+} + \frac{S^{+3}}{H^+} \ ; \tag{19}$$

$$\frac{Ar}{H} = \frac{Ar^+}{H^+} + \frac{Ar^{++}}{H^+} . \tag{20}$$

The grid of photoionization models described in Sect. 5.2 allows us to verify the validity of the above expressions (cf. Fig. 12). The ionization correction factor for Ne is ∼1 for all the sources. Ar^{+3} may be present in the higher ionized sources (photons with energies >40.7 eV are necessary to ionize Ar^{++} to Ar^{+3}, roughly the same energies to produce Ne^{++}). However, the contribution of this ion is estimated to be <30%. The S abundance is always underestimated by ∼15%. Table 9 gives the ionic and total elemental abundances for argon, sulphur and neon. The uncertainties are derived propagating the line flux errors.

Figure 18 shows Ne/H and Ar/H as a function of R_{Gal}. Clear gradients with galactocentric distance can be observed for both species. Linear least squares fits to the neon and argon abundances, displayed as solid lines in Fig. 18, are:

$$\log\frac{Ne}{H} = (-3.49 \pm 0.06) - (0.039 \pm 0.007)R_{Gal} \tag{21}$$

and

$$\log\frac{Ar}{H} = (-5.10 \pm 0.09) - (0.045 \pm 0.011)R_{Gal} \ , \tag{22}$$

with correlation coefficients $r = -0.76$ and -0.66, respectively.
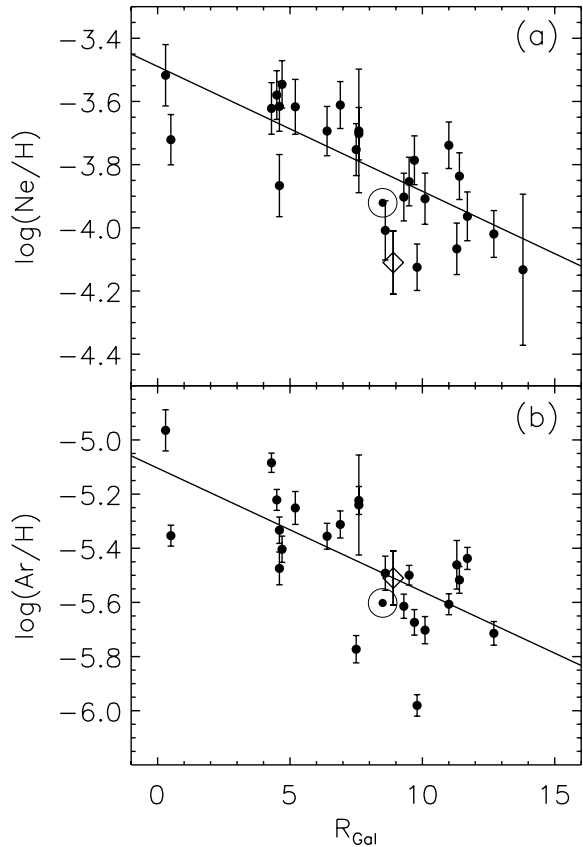

Fig. 18. Total abundances of **a)** neon and **b)** argon as a function of R_{Gal}. The solar abundance (Grevesse & Sauval 1998) is indicated by the symbol ⊙ and the Orion abundance (Esteban et al. 1998) by an open diamond.

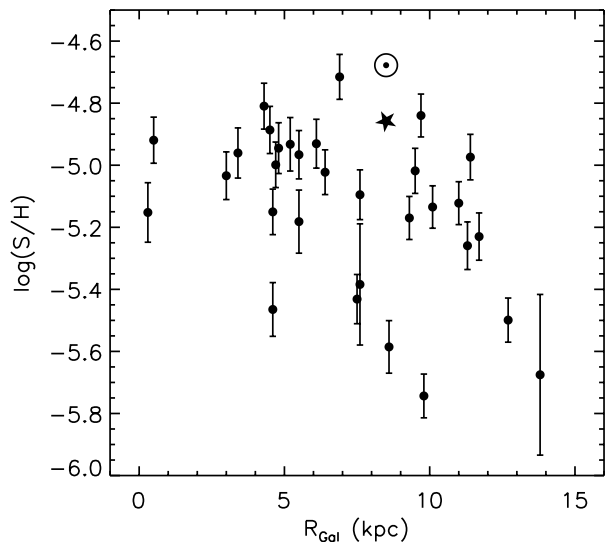**Fig. 19.** S/H abundance as a function of R_{Gal}. The solar abundance (Grevesse & Sauval 1998) is indicated by the symbol ⊙ and the interstellar abundance (Snow & Witt 1996) by a star. As discussed in Sect. 7.3, S/H could be underestimated by up to a factor 4 due to the T_e and n_e uncertainties.

We note that an electron temperature gradient in the Galaxy may systematically enlarge the above derived

elemental abundance gradients. Specifically, if we correct for a T_e gradient given by $T_e = 5000 + 5000\times(R_{Gal}(\mathrm{kpc})/15)$, based on the T_e gradients derived by Shaver et al. (1983), Afflerbach et al. (1996) and Deharveng et al. (2000), the slopes in the Ne/H and Ar/H gradients become -0.06 and -0.07 dex kpc^{-1}, respectively.

While Ar/H and Ne/H are T_e-dependent through the Brα line emissivity, the ratio Ar/Ne is practically insensitive to changes in T_e. An approximately constant Ar/Ne close to solar is found, contrary to the tentative Ar/Ne galactic gradient derived from a small sample of KAO observations (Simpson et al. 1995a).

S/H abundances are plotted in Fig. 19. No meaningful Galactic gradient is seen for S/H and a very large dispersion is found at any given R_{Gal}, unlike the smaller dispersion in the Ar/H or Ne/H Galactic abundances. The absolute abundances are also improbably low compared to the solar and interstellar abundances – on average 2 times lower that the IS sulphur abundance by Snow & Witt (1996); a factor of 5 for the extreme cases –, since sulphur is not expected to be strongly depleted into grains. However, the quoted sulphur abundances do not include the systematic uncertainties due to the effect of electron temperature and density (cf. Sect. 5). In view of the rms densities derived from the radio observations (we note that the sources with the lower S/H abundances also have very high $n_{e,rms} > 10^4$ cm^{-3}) and the T_e gradient in the Galaxy, we estimate that the S abundances are underestimated by up to a factor 4.

7.4. Comparison of gradients with previous studies

Figure 20 compares the gradient slopes derived for N/O, Ne/H and Ar/H with previous determinations using H II regions – optical (Shaver et al. 1983), IRAS (Simpson & Rubin 1990), KAO (Simpson et al. 1995b) –, disk planetary nebulae of type II (Maciel & Quireza 1999) and B stars (Smartt et al. 2001).

Good agreement is found for N/O and Ar/H. Our Ne/H gradient matches the one found from planetary nebula, but is flatter than the previous infrared determinations using IRAS and KAO. Both IRAS and KAO determinations agree, however. We note that both relied on radio data to derive the abundances and therefore, did not suffer much from the systematic electron temperature uncertainty, while our gradients have been probably depressed because of the assumption of a single $T_e = 7500$ K. Indeed, if we correct our derived Ne/H gradient from the T_e gradient in the Galaxy (the open stars in Fig. 20), then we are in reasonable agreement with both IRAS and KAO.

8. Summary and conclusions

Based on the ISO spectral catalogue of compact H II regions by Peeters et al. (2002), a first analysis of the hydrogen recombination and atomic fine-structure lines
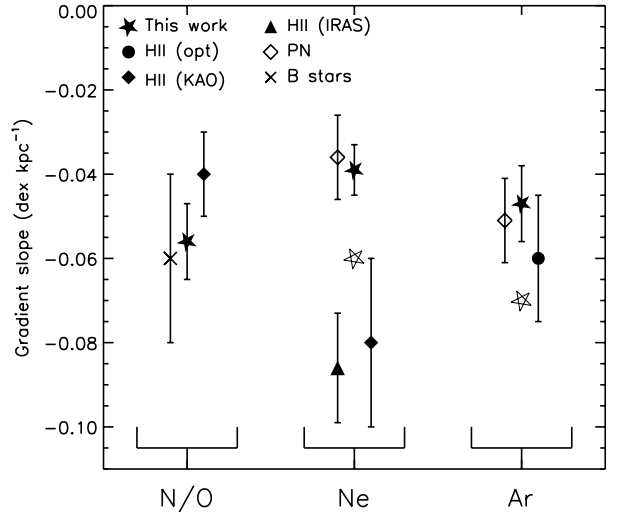

Fig. 20. Comparison of the derived gradient slopes for N/O, Ne/H and Ar/H with previous determinations using H II regions – optical (Shaver et al. 1983), IRAS (Simpson & Rubin 1990), KAO (Simpson et al. 1995b) –, disk planetary nebulae of type II (Maciel & Quireza 1999) and B stars (Smartt et al. 2001). The open stars indicate the slopes obtained when a Galactic T_e gradient of $\sim$330 K kpc^{-1} is assumed.

originated in the ionized gas has been presented. The main results of this study are:

• The SWS H I recombination lines between 2 and 8 μm have been used to estimate the extinction law at these wavelengths for 14 H II regions. An extinction in the K band between 0 and $\sim$3 mag has been derived.

• The electron densities determined by the [O III] 88/52 μm line ratio, in between $\sim$100 and 3000 cm^{-3}, are shown to be substantially smaller than the rms densities resulting from radio continuum observations. This fact suggests that the ultracompact cores observed in the radio have a region of less dense gas (traced by [O III] 88/52 μm) at high excitation, which could be produced by leakage of radiation from the ultracompact region. This low density gas might be identified with the physically related, low brightness envelopes recently mapped in radio around ultracompact H II regions (Kurtz et al. 1999; Kim & Koo 2001).

• Significant variations are found in the degree of ionization of the H II regions as measured by the ratios Ar^{++}/Ar$^+$, N^{++}/N$^+$, S^{+3}/S^{++} and Ne^{++}/Ne$^+$. These ratios, which span a range of ionization potential up to 41 eV, correlate well with each other, suggesting that the spectral hardening affects equally the full range of ionizing energies. In addition, the ionic ratios vary with R_{Gal}, with the H II regions in the outer Galaxy being powered by a seemingly harder radiation field. This increase in degree of ionization, i.e. in properties of the ionizing star, could be related to the metallicity gradient. However, the precise mechanism coupling the stellar characteristics to the elemental abundances remains unclear. Elemental abundances may couple directly to the stellar

Table 9. Ionic and total abundances of neon, sulphur and argon derived in the low density limit and assuming a single $T_e = 7500$ K. Systematic uncertainties may affect these abundances because of the T_e Galactic gradient. Sulphur abundances for some sources could be underestimated by up to a factor 4 due to the T_e and n_e uncertainties (see Sect. 7.3).

Source	NEON			SULPHUR			ARGON		
	Ne^+/H^+ $\times 10^{-4}$	Ne^{++}/H^+ $\times 10^{-4}$	Ne/H $\times 10^{-4}$	S^{++}/H^+ $\times 10^{-6}$	S^{+3}/H^+ $\times 10^{-6}$	S/H $\times 10^{-6}$	Ar^+/H^+ $\times 10^{-6}$	Ar^{++}/H^+ $\times 10^{-6}$	Ar/H $\times 10^{-6}$
IR 01045	0.6 ± 0.3	0.16 ± 0.09	0.7 ± 0.4	$2. \pm 1.$	<0.1	$2. \pm 1.$	$<.6$	<0.5	$<1.$
IR 02219	0.9 ± 0.2	0.9 ± 0.2	1.8 ± 0.3	$7. \pm 1.$	0.90 ± 0.09	$8. \pm 1.$	0.36 ± 0.03	2.1 ± 0.2	2.5 ± 0.2
IR 02575	<0.1	<0.04	<0.1	<0.5	<0.09	<0.6	<0.5	<0.3	<0.8
IR 10589	1.2 ± 0.2	0.16 ± 0.03	1.4 ± 0.2	$9. \pm 2.$	0.18 ± 0.03	$10. \pm 2.$	1.7 ± 0.1	1.5 ± 0.2	3.2 ± 0.3
IR 11143	0.54 ± 0.10	1.1 ± 0.2	1.6 ± 0.3	$12. \pm 2.$	2.6 ± 0.3	$14. \pm 2.$	<0.2	2.1 ± 0.2	2.1 ± 0.2
IR 12063	0.7 ± 0.1	0.59 ± 0.10	1.3 ± 0.2	5.8 ± 1.0	0.92 ± 0.09	$7. \pm 1.$	0.43 ± 0.05	2.0 ± 0.2	2.4 ± 0.3
IR 12073	0.34 ± 0.06	0.9 ± 0.2	1.2 ± 0.2	5.4 ± 1.0	1.9 ± 0.2	$7. \pm 1.$	0.12 ± 0.04	1.9 ± 0.2	2.0 ± 0.2
IR 12331	1.9 ± 0.3	0.59 ± 0.10	2.4 ± 0.4	$19. \pm 3.$	0.53 ± 0.05	$19. \pm 3.$	1.6 ± 0.2	3.3 ± 0.4	4.9 ± 0.6
IR 15384	1.8 ± 0.3	0.25 ± 0.05	2.0 ± 0.4	$9. \pm 2.$	0.19 ± 0.02	$9. \pm 2.$	2.6 ± 0.2	1.8 ± 0.3	4.4 ± 0.5
IR 15502	1.2 ± 0.3	0.13 ± 0.03	1.4 ± 0.3	3.4 ± 0.7	0.033 ± 0.006	3.4 ± 0.7	2.7 ± 0.4	0.6 ± 0.1	3.4 ± 0.5
IR 17221	2.4 ± 0.5	0.04 ± 0.01	2.4 ± 0.5	$12. \pm 2.$	0.044 ± 0.010	$12. \pm 2.$	4.4 ± 0.6	1.2 ± 0.2	5.6 ± 0.8
Sgr C	3.0 ± 0.7	<0.05	3.0 ± 0.7	$7. \pm 2.$	<0.08	$7. \pm 2.$	$11. \pm 2.$	<0.4	$11. \pm 2.$
IR 17455	1.6 ± 0.3	0.31 ± 0.05	1.9 ± 0.3	$12. \pm 2.$	0.19 ± 0.03	$12. \pm 2.$	2.7 ± 0.2	1.8 ± 0.2	4.4 ± 0.4
IR 18032	2.0 ± 0.4	<0.02	2.0 ± 0.4	$8. \pm 1.$	<0.03	$8. \pm 1.$	5.3 ± 0.6	0.71 ± 0.09	6.0 ± 0.7
IR 18116	2.3 ± 0.4	0.08 ± 0.02	2.4 ± 0.4	$15. \pm 3.$	<0.03	$15. \pm 3.$	7.4 ± 0.6	0.9 ± 0.1	8.2 ± 0.7
IR 18317	2.6 ± 0.5	0.08 ± 0.01	2.6 ± 0.5	$13. \pm 2.$	0.034 ± 0.009	$13. \pm 2.$	4.9 ± 0.4	1.1 ± 0.1	6.0 ± 0.5
IR 18434	2.2 ± 0.4	0.26 ± 0.05	2.4 ± 0.4	$7. \pm 1.$	0.13 ± 0.02	$7. \pm 1.$	3.0 ± 0.3	1.7 ± 0.2	4.6 ± 0.5
IR 18479	1.5 ± 0.3	0.30 ± 0.06	1.8 ± 0.3	3.7 ± 0.7	<0.05	3.7 ± 0.7	1.7 ± 0.2	<0.2	1.7 ± 0.2
IR 18502	2.6 ± 0.4	0.26 ± 0.05	2.8 ± 0.5	$10. \pm 2.$	0.12 ± 0.02	$10. \pm 2.$	2.9 ± 0.3	1.1 ± 0.1	3.9 ± 0.4
IR 19442	2.0 ± 0.9	<0.03	2.0 ± 0.9	$4. \pm 2.$	<0.1	$4. \pm 2.$	$6. \pm 2.$	<0.3	$6. \pm 2.$
IR 19598	0.37 ± 0.06	0.38 ± 0.06	0.8 ± 0.1	1.7 ± 0.3	0.15 ± 0.01	1.8 ± 0.3	0.43 ± 0.03	0.61 ± 0.06	1.05 ± 0.10
DR 21	0.9 ± 0.2	0.11 ± 0.05	1.0 ± 0.2	2.6 ± 0.5	<0.02	2.6 ± 0.5	2.9 ± 0.4	0.35 ± 0.07	3.2 ± 0.5
IR 21190	0.7 ± 0.1	0.29 ± 0.05	1.0 ± 0.2	3.0 ± 0.5	0.20 ± 0.02	3.2 ± 0.5	0.50 ± 0.06	1.4 ± 0.1	1.9 ± 0.2
IR 22308	0.9 ± 0.2	<0.02	0.9 ± 0.2	5.5 ± 1.0	<0.05	5.5 ± 1.0	2.8 ± 0.5	0.6 ± 0.2	3.5 ± 0.7
IR 23030	1.4 ± 0.2	0.09 ± 0.01	1.5 ± 0.2	$10. \pm 2.$	0.17 ± 0.02	$11. \pm 2.$	1.0 ± 0.1	2.0 ± 0.2	3.0 ± 0.3
IR 23133	1.1 ± 0.2	<0.01	1.1 ± 0.2	$6. \pm 1.$	0.025 ± 0.006	$6. \pm 1.$	2.9 ± 0.3	0.73 ± 0.08	3.7 ± 0.3

atmosphere opacity which controls the flux and its dependence on the frequency. Qualitatively, theoretical models support this coupling (e.g. Balick & Sneden 1976). The opacity by trace ions also controls the stellar wind, which in their turn have a major influence on the emerging stellar flux. Again, models show qualitative agreement (e.g. Schaerer & de Koter 1997). Third, the connection between elemental abundances and stellar flux may be indirect. For example, the elemental abundance may control the dust opacity and thereby the mass of the star formed because of radiation pressure effects during the collapse phase (cf. Kahn 1974; Shields & Tinsley 1976). Last, the hardening of the radiation field with R_{Gal} may reflect a systematic variation in the "age" of the star powering the H II regions. Possibly, in the inner parts of the Galaxy ionizing stars evolve more "rapidly" (i.e. are cooler for the same luminosity) than in the outer Galaxy. In that respect, the detailed photoionized model for the H II region IRAS 18434−0242 (G29.96−0.02), using recent line-blanketed, non-LTE stellar atmosphere models including winds (Schaerer & de Koter 1997), finds good agreement with all the ion pair ratios using a luminous star which has already evolved off the main sequence (Paper III). In such a model, the variations in the degree of ionization with R_{Gal} might reflect a selection effect in our sample where, for example, the rate of expansion of the compact H II region is linked to the environment (ie. metallicity).

● A gradient in N^{++}/O^{++} is observed in the sense of a decreasing ionic abundance ratio with R_{Gal}. This observed ionic abundance ratio N^{++}/O^{++} has been converted into the elemental abundance ratio N/O using the observed ionization ratio Ne^{++}/Ne^+, sensitive to the ionization state of the H II region, and detailed photoionization model calculations. The N/O abundance ratio also shows a decrease with R_{Gal}, although shallower than in the case of N^{++}/O^{++}, pointing to the existence of an intrinsic variation in the gas phase N/O abundance. Thus, there seems to be an important contribution to the synthesis of nitrogen by secondary production. The derived slope for N/O ($\Delta \log N/O = -0.056 \pm 0.009 \, \mathrm{dex \, kpc^{-1}}$) is in agreement with previous H II regions (e.g. Simpson et al. 1995b) and B stars (e.g. Smartt et al. 2001) determinations.

• Our analysis method underestimated the sulphur abundances by up to a factor 4 and hence, no meaningful Galactic gradient could be derived. We estimated a lower limit for the oxygen abundance through the derivation of O^{++}/H^+. We miss the important O II ionization stage, which does not have any infrared fine-structure line. On the other hand, because the [N II] 122 μm line is very weak and it was only detected in a limited number of sources, and no radio information was available for all these sources, N/H could only be determined for a few sources and therefore, a gradient could not be drawn. We found, however, supersolar nitrogen abundances for the sources in the inner 5 kpc.

• The total elemental abundances of neon and argon with respect to H have been also derived. Ne/H and Ar/H have been found to decrease with the galactocentric distance as $\Delta \log \mathrm{Ne/H} = -0.039 \pm 0.007\,\mathrm{dex\,kpc^{-1}}$ and $\Delta \log \mathrm{Ar/H} = -0.045 \pm 0.011\,\mathrm{dex\,kpc^{-1}}$. The slopes of neon and argon coincide within the uncertainties, indicating that both species have a similar stellar nucleosynthesis history. However, the existence of a Galactocentric T_e gradient may enlarge these elemental gradients. Because only a few radio recombination line observations towards the H II regions, which can be used to characterize the nebular T_e, are available, we do not have enough information to correct individually the derived abundances. However, adopting a decrease in T_e of $\sim$330 K kpc^{-1} with galactocentric distance, we estimate that the slopes for the Ne/H and Ar/H gradients become -0.06 and -0.07 dex kpc^{-1}, respectively. These corrected slopes are in reasonable agreement with the previous determinations by IRAS (Simpson & Rubin 1990) and KAO (Simpson et al. 1995b). Ar/Ne, which is independent of T_e, is found to be approximately solar and constant with R_{Gal}.

The complete infrared spectra from 2.3 to 196 μm provided by the ISO catalogue of galactic H II regions (Peeters et al. 2002) has allowed us to study the ionizing conditions in these sources and derive relative and absolute elemental abundances across the Galactic disk. The first analysis presented in this paper has shown that useful conclusions can be drawn from these data. However, there are still open issues and to improve on the present results additional information is required. In particular, the detailed knowledge of the extent and relative spatial distributions of the fine-structure atomic lines is lacking for almost all the compact H II regions. The knowledge of the electron temperature is also critical in refining the elemental abundances. Observations of radio recombinations lines will be helpful to estimate T_e for all the sources discussed in this paper and to correct for the T_e dependence.

References

Afflerbach, A., Churchwell, E., Acord, J. M., et al. 1996, ApJS, 106, 423

Afflerbach, A., Churchwell, E., & Werner, M. W. 1997, ApJ, 478, 190

Armand, C., Baluteau, J.-P., Joubert, M., Gry, C., & Cox, P. 1996, A&A, 306, 593

Balick, B., & Sneden, C. 1976, ApJ, 208, 336

Barsony, M. 1989, ApJ, 345, 268

Becker, R. H., White, R. L., Helfand, D. J., & Zoonematkermani, S. 1994, ApJS, 91, 347

Biemont, E., & Bromage, G. E. 1983, MNRAS, 205, 1085

Blum, R. D., & Pradhan, A. K. 1992, ApJS, 80, 425

Butler, K., & Zeippen, C. J. 1994, A&AS, 108, 1

Copetti, M. V. F., Mallmann, J. A. H., Schmidt, A. A., & Castañeda, H. O. 2000, A&A, 357, 621

Deharveng, L., Peña, M., Caplan, J., & Costero, R. 2000, MNRAS, 311, 329

Dickel, H. R., Dickel, J. R., Wilson, W. J., & Werner, M. W. 1980, ApJ, 237, 711

Draine, B. T. 1985, ApJS, 57, 587

Draine, B. T. 1989, in Infrared Spectroscopy in Astronomy, ESA SP–290, 93–98

Esteban, C., Peimbert, M., Torres-Peimbert, S., & Escalante, V. 1998, MNRAS, 295, 401

Fey, A. L., Gaume, R. A., Claussen, M. J., & Vrba, F. J. 1995, ApJ, 453, 308

Fich, M. 1986, AJ, 92, 787

Fich, M. 1993, ApJS, 86, 475

Fich, M. & Silkey, M. 1991, ApJ, 366, 107

Fitzsimmons, A., Dufton, P. L., & Rolleston, W. R. J. 1992, MNRAS, 259, 489

Galavís, M. E., Mendoza, C., & Zeippen, C. J. 1995, A&AS, 111, 347

Galavís, M. E., Mendoza, C., & Zeippen, C. J. 1997, A&AS, 123, 159

Galavís, M. E., Mendoza, C., & Zeippen, C. J. 1998a, A&AS, 131, 499

Galavís, M. E., Mendoza, C., & Zeippen, C. J. 1998b, A&AS, 133, 245

Garay, G., Rodriguez, L. F., Moran, J. M., & Churchwell, E. 1993, ApJ, 418, 368

Grevesse, N. & Sauval, A. J. 1998, Space Sci. Rev., 85, 161

Gummersbach, C. A., Kaufer, A., Schaefer, D. R., Szeifert, T., & Wolf, B. 1998, A&A, 338, 881

Hackwell, J. A., Gehrz, R. D., Smith, J. R., & Briotta, D. A. 1978, ApJ, 221, 797

Harris, S. & Wynn-Williams, C. G. 1976, MNRAS, 174, 649

Hayward, T. L., Grasdalen, G. L., Woodward, C. E., et al. 1989, ApJ, 345, 894

Howard, E. M., Pipher, J. L., Forrest, W. J., & de Pree, C. G. 1996, ApJ, 460, 744

Hummer, D. G., & Storey, P. J. 1987, MNRAS, 224, 801

Isaacman, R. 1984, MNRAS, 208, 399

Kafatos, M., & Lynch, J. P. 1980, ApJS, 42, 611

Kahn, F. D. 1974, A&A, 37, 149

Kim, K., & Koo, B. 2001, ApJ, 549, 979

Kurtz, S., Churchwell, E., & Wood, D. O. S. 1994, ApJS, 91, 659

Kurtz, S. E., Watson, A. M., Hofner, P., & Otte, B. 1999, ApJ, 514, 232

Lennon, D. J., & Burke, V. M. 1994, A&AS, 103, 273

Lester, D. F., Dinerstein, H. L., Werner, M. W., et al. 1987, ApJ, 320, 573

Liszt, H. S., & Spiker, R. W. 1995, ApJS, 98, 259

Maciel, W. J., & Koppen, J. 1994, A&A, 282, 436

Maciel, W. J., & Quireza, C. 1999, A&A, 345, 629

Martin, P. G., & Whittet, D. C. B. 1990, ApJ, 357, 113

Mathis, J. S. 1990, ARA&A, 28, 37

McCutcheon, W. H., Sato, T., Dewdney, P. E., & Purton, C. R. 1991, AJ, 101, 1435

McLaughlin, B. M., & Bell, K. L. 2000, J. Phys. B, 33, 597

Mehringer, D. M. 1994, ApJS, 91, 713

Mendoza, C. 1983, in Planetary Nebulae, IAU Symp., 103, 143

Mendoza, C., & Zeippen, C. J. 1983, MNRAS, 202, 981

Mezger, P. G., & Henderson, A. P. 1967, ApJ, 147, 471

Morisset, C., Baluteau, J.-P., Schaerer, D., et al. 2001, A&A, submitted (Paper III)

Morisset, C., & Pequignot, D. 1996, A&A, 312, 135

Osterbrock, D. E. 1989, Astrophysics of gaseous nebulae and active galactic nuclei (Research supported by the University of California, John Simon Guggenheim Memorial Foundation, University of Minnesota, et al. Mill Valley, CA, University Science Books)

Peeters, E., Martín-Hernández, N. L., Damour, F., et al. 2002, A&A, 381, 571 (Paper I)

Pelan, J., & Berrington, K. A. 1995, A&AS, 110, 209

Pratap, P., Megeath, S. T., & Bergin, E. A. 1999, ApJ, 517, 799

Roelfsema, P. R., & Goss, W. M. 1991, A&AS, 87, 177

Roelfsema, P. R., Goss, W. M., & Geballe, T. R. 1989, A&A, 222, 247

Rolleston, W. R. J., Smartt, S. J., Dufton, P. L., & Ryans, R. S. I. 2000, A&A, 363, 537

Rubin, R. H., Dufour, R. J., Colgan, S. W. J., et al. 2000, in Ionized Gaseous Nebulae. Mexico City November 21–24, 2000, E51

Rubin, R. H., Simpson, J. P., Erickson, E. F., & Haas, M. R. 1988, ApJ, 327, 377

Rubin, R. H., Simpson, J. P., Lord, S. D., et al. 1994, ApJ, 420, 772

Rudolph, A. L., Brand, J., de Geus, E. J., & Wouterloot, J. G. A. 1996, ApJ, 458, 653

Rudolph, A. L., Simpson, J. P., Haas, M. R., Erickson, E. F., & Fich, M. 1997, ApJ, 489, 94

Saraph, H. E., & Storey, P. J. 1999, A&AS, 134, 369

Saraph, H. E., & Tully, J. A. 1994, A&AS, 107, 29

Schaerer, D., & de Koter, A. 1997, A&A, 322, 598

Shaver, P. A., McGee, R. X., Newton, L. M., Danks, A. C., & Pottasch, S. R. 1983, MNRAS, 204, 53

Shields, G. A., & Tinsley, B. M. 1976, ApJ, 203, 66

Simpson, J. P., Bregman, J. D., Dinerstein, H. L., et al. 1995a, in ASP Conf. Ser. 73, From Gas to Stars to Dust, 105

Simpson, J. P., Colgan, S. W. J., Rubin, R. H., Erickson, E. F., & Haas, M. R. 1995b, ApJ, 444, 721

Simpson, J. P., & Rubin, R. H. 1990, ApJ, 354, 165

Smartt, S. J., & Rolleston, W. R. J. 1997, ApJ, 481, L47

Smartt, S. J., Venn, K. A., Dufton, P. L., et al. 2001, A&A, 367, 86

Snow, T. P., & Witt, A. N. 1996, ApJ, 468, L65

Stasińska, G., & Schaerer, D. 1997, A&A, 322, 615

Tayal, S. S., & Gupta, G. P. 1999, ApJ, 526, 544

Tieftrunk, A. R., Gaume, R. A., Claussen, M. J., Wilson, T. L., & Johnston, K. J. 1997, A&A, 318, 931

Tielens, A. G. G. M., & Hollenbach, D. 1985, ApJ, 291, 722

Vila-Costas, M. B., & Edmunds, M. G. 1992, MNRAS, 259, 121

Vílchez, J. M., & Pagel, B. E. J. 1988, MNRAS, 231, 257

Watson, A. M., Coil, A. L., Shepherd, D. S., Hofner, P., & Churchwell, E. 1997, ApJ, 487, 818

Wood, D. O. S., & Churchwell, E. 1989, ApJS, 69, 831

Zaritsky, D., Kennicutt, R. C., & Huchra, J. P. 1994, ApJ, 420, 87